

Linear dynamics of flexible multibody systems : a system-based approach

Jawhar Chebbi, Vincent Dubanchet, José Alvaro Perez Gonzalez, Daniel Alazard

▶ **To cite this version:**

Jawhar Chebbi, Vincent Dubanchet, José Alvaro Perez Gonzalez, Daniel Alazard. Linear dynamics of flexible multibody systems : a system-based approach. Multibody System Dynamics, 2016, pp.0. 10.1007/s11044-016-9559-y . hal-01405184

HAL Id: hal-01405184
https://hal.science/hal-01405184

Submitted on 9 Dec 2016

HAL is a multi-disciplinary open access archive for the deposit and dissemination of scientific research documents, whether they are published or not. The documents may come from teaching and research institutions in France or abroad, or from public or private research centers.

L'archive ouverte pluridisciplinaire **HAL**, est destinée au dépôt et à la diffusion de documents scientifiques de niveau recherche, publiés ou non, émanant des établissements d'enseignement et de recherche français ou étrangers, des laboratoires publics ou privés.



Open Archive TOULOUSE Archive Ouverte (OATAO)

OATAO is an open access repository that collects the work of Toulouse researchers and makes it freely available over the web where possible.

This is an author-deposited version published in: http://oatao.univ-toulouse.fr/
Eprints ID: 16559

To link this article: http://dx.doi.org/10.1007/s11044-016-9559-y

To cite this version: Chebbi, Jawhar and Dubanchet, Vincent and Perez Gonzalez, José Alvaro and Alazard, Daniel Linear dynamics of flexible multibody systems. (2016) Multibody System Dynamics. ISSN 1384-5640

Any correspondence concerning this service should be sent to the repository administrator: staff-oatao@listes-diff.inp-toulouse.fr

Linear dynamics of flexible multibody systems

A system-based approach

Jawhar Chebbi[1] · **Vincent Dubanchet**[1] · **José Alvaro Perez Gonzalez**[1] · **Daniel Alazard**[1]

Abstract We present a new methodology to derive a linear model of flexible multibody system dynamics. This approach is based on the two-port model of each body allowing the model of the whole system to be built just connecting the inputs/outputs of each body model. Boundary conditions of each body can be taken into account through inversion of some input–output channels of its two-port model. This approach is extended here to treat the case of closed-loop kinematic mechanisms. Lagrange multipliers are commonly used in an augmented differential-algebraic equation to solve loop-closure constraints. Instead, they are considered here as a model output that is connected to the adjoining body model through a feedback. After a summary of main results in the general case, the case of planar mechanisms with multiple uniform beams is considered, and the two-port model of the Euler–Bernoulli beam is derived. The choice of the assumed modes is then discussed regarding the accuracy of the first natural frequencies for various boundary conditions. The overall modeling approach is then applied to the well-known four-bar mechanism.

Keywords Flexible structure · Multibody system · Linear system

1 Introduction

Dynamics of flexible multibody systems has been vigorously studied over the last decades in connection with various application fields such as light weight robotic arm, rotating machinery, helicopter rotor with flexible blades, large flexible space structures, and so on. We can find hundreds of papers about the writing, solving, and simulation of the differential and algebraic equations governing the dynamics of flexible multibody systems [21, 22]. We can distinguish methods used to build a validation model including nonlinear terms (centrifugal, Coriolis) [4, 12] and methods used to derive a preliminary design model, which can be also used for control design [10, 14]. The latter often focus on the linear behavior of flexible multibody systems under a small displacement assumption. Link flexibility is

✉ D. Alazard
alazard@isae.fr

[1] ISAE-SUPAERO, Toulouse, France

approximated by discretized models using finite element methods (FEM) or assumed mode methods (AMM) [28]. The model of the whole multibody system is then derived using the Euler–Lagrange formalism. For example, in space applications, considering a flexible robotic arm fitted on a chaser spacecraft, the inertial load seen from the tip of a flexible link can vary considerably according to the geometrical configuration of the robotic arm. The AMM is then often used [4, 28] with the first *clamped–mass* eigenfunctions. The main drawback is that the *mass* must be a time-variant parameter and need to be updated along with the geometrical configuration. Otherwise, an approximation by an average value is still possible. However, if we consider the capture of a massive space debris, then the boundary conditions at the tips of each flexible link may be closer to the *clamped–clamped* condition than to the *clamped–mass* condition. During the preliminary design study of such a system, we can argue that the system dynamics is more sensitive to such a change in the boundary conditions than in the effects of nonlinear terms. Thus, there is a real need to have a model for each link or substructure that is valid for arbitrary boundary conditions before doing the assembly of the whole structure.

Among all substructuring approaches, the transfer matrix method (TMM) has motivated lots of literature during last decades. Leckie [11] stated the fundamentals of this method: the transfer matrix is a relation between the left point and right point state vectors of a flexible body. The state vector at a point is defined as the augmented vector composed of the generalized displacements and the corresponding generalized forces. This method was particularly well suited for modeling structures composed of serially connected bodies or open-chain-like structures. Later, this approach was merged with the finite-element (FE) method and presented as the FE-TM method [5]. The FE-TM method was first developed in [13] to provide reduced models using a condensation procedure, before being extended in [19] for complex shape bodies to reduce computation efforts in solving eigenvalue problems. Some extensions were also developed for control design purposes [27], including noncollocated feedback [10], and for hybrid (rigid and flexible) multibody systems [20]. In [9], the TMM was applied to a closed-loop kinematic chain of flexible bodies and more particularly to the four-bar mechanism. Nevertheless, the TMM has some limitations due to the inversion of submatrices, which are not always square or invertible, depending on the boundary conditions [27]. Furthermore, another limitation comes from the fact that this method cannot be directly applied to tree-like structures, like a spacecraft composed of a main rigid body fitted with several flexible appendages (solar panels, antenna, etc.). In such a case, the objective of the modeling is to find a relation between the generalized forces and displacements at the root of the tree-like structure, that is, the main body. Such a model is required for the design of the attitude and orbit control system (AOCS). Some alternatives and efficient approaches were developed to treat that case. They are based on the effective mass/inertia model of each flexible appendage (i.e., the relation between forces and accelerations at the anchorage point of the appendage on the main body) [7] or also on the impedance matrix [15, 26]. These methods were first introduced in [3] to analyze dynamic coupling between substructures through the component mode synthesis (CMS) and are commonly used in space engineering [8]. The limitation of the effective mass/inertia approach is the loss of appendage information beyond the anchorage point, such as the deflection at the free tip. Therefore, such a method cannot be applied to model an arbitrary chain-like structure of flexible bodies.

The main contribution of this paper is to propose a system-based approach to model the linear dynamic behavior of a flexible link in a multibody system. This approach is independent of the boundary conditions applied at the connecting points of this link. The inputs and outputs of this model, named two-input–two-output port (TITOP) model, are the forces

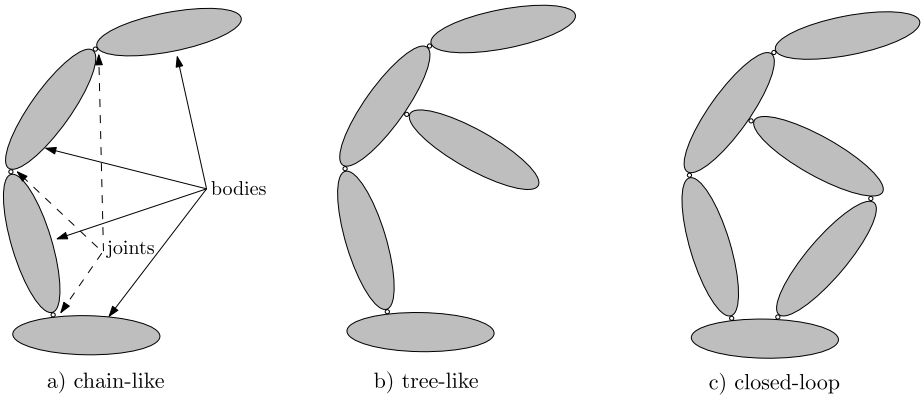


Fig. 1 Multibody systems

and accelerations at the connecting points of the link with its neighbors. This model embeds, in the same minimal state-space representation, the direct and the inverse dynamic models of the link. Its various input–output channels (or ports) are thus invertible. By applying very simple channel inversion operations this model can be directly plugged into the whole multibody system model, seen as a block-diagram model. The boundary conditions at a connecting point of the link are seen as an external feedback loop between forces and accelerations. The same model of the link can be used for any kind of open-loop or closed-loop kinematic mechanisms involving this link. This method fills the gap between the TM method and the effective mass-inertia method. Note that from the terminology point of view, what is called the state vector of left and right points in the TM approach are in fact the inputs and outputs of the transfer matrix. These inputs and outputs are completely revisited in the TITOP approach. Finally, accelerations at the connecting points are considered instead of generalized displacements. The state vector is now the vector of variables associated to the minimal state-space representation of the TITOP model (which is twice the number of flexible modes of the considered body). First introduced in [1], the TITOP model approach is also illustrated on space engineering applications in [14, 16–18].

In Sect. 2, the main results of [1] are summarized and reformulated in the context of general multibody system with a focus on closed-loop mechanisms. In Sect. 3, the TITOP model is derived for an Euler–Bernoulli beam. It will be shown that the first two natural frequencies for any kind of tip conditions are accurately modeled from the simple TITOP approach. In Sect. 4, the methodology is then applied to the well-known four-bar mechanism: the first natural frequencies and modal shapes are analyzed versus the crank angle and compared with the results already published [9], [29].

2 Two-port model approach

An N degrees-of-freedom (d.o.f.) multibody system can be divided into bodies (or links) connected to each other by (prismatic, revolute, cardan, spherical) joints. We can distinguish chain-like multibody systems (Fig. 1a), tree-like systems (Fig. 1b), and closed-loop kinematic systems (Fig. 1c). In all the cases, the objective of this paper is to derive the linear model of the system dynamics around a given equilibrium configuration of N d.o.f.,

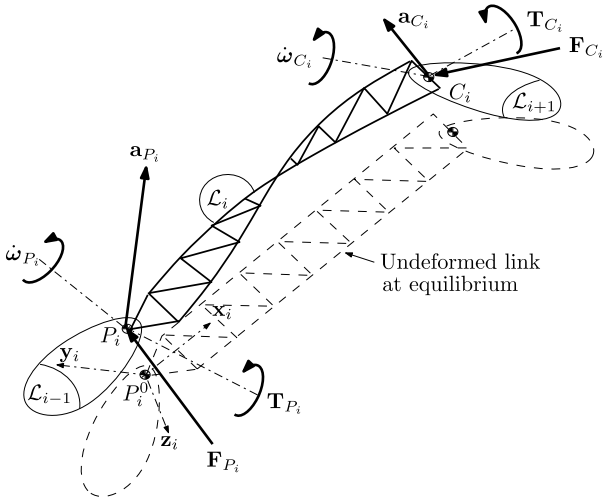


Fig. 2 The ith flexible link in the structure

$\boldsymbol{\theta} = [\theta_1, \theta_2, \ldots, \theta_N]^T$ and $\dot{\boldsymbol{\theta}} = \mathbf{0}$, assuming small variations of the d.o.f. around this configuration and small deformations of flexible links. Therefore, the Coriolis and centrifugal forces are neglected throughout this paper.

Frame definition Under this small displacement assumption, it is possible to define an inertial frame $\mathcal{R}_i = (P_i^0, \mathbf{x}_i, \mathbf{y}_i, \mathbf{z}_i)$ attached to the equilibrium configuration of each link i. In the chain-like and tree-like cases, P_i^0 is the connection point of link i with the parent link at the equilibrium. $\mathbf{P}_{i/j}$ is the direction cosine matrix (DCM) between frames $\mathcal{R}_i$ and $\mathcal{R}_j$ (i.e., the matrix of components of unitary vectors $\mathbf{x}_j, \mathbf{y}_j, \mathbf{z}_j$ in $\mathcal{R}_i$). $\mathbf{P}_{i/j}$ depends only on the given configuration $\boldsymbol{\theta}$ for all i and j.

2.1 Two-port model of a link

The link $\mathcal{L}_i$ connected to the parent substructure $\mathcal{L}_{i-1}$ at the point P_i and to the child substructure $\mathcal{L}_{i+1}$ at point C_i is depicted in Fig. 2. The double-port or TITOP (two-input–two-output port) model $\mathbf{G}^{\mathcal{L}_i}_{P_i,C_i}(s)$, proposed in [1], is a linear dynamic model between 12 inputs:

- the six components in $\mathcal{R}_i$ of the wrench $\mathbf{W}_{C_i} = [\mathbf{F}_{C_i}^T \mathbf{T}_{C_i}^T]^T$ applied by the substructure $\mathcal{L}_{i+1}$ to the link $\mathcal{L}_i$ at point C_i: $\mathbf{F}_{C_i}$ stands for the three-component force vector applied at point C_i, and $\mathbf{T}_{C_i}$ stands for the three-component torque vector applied at point C_i,
- the six components in $\mathcal{R}_i$ of the acceleration twist $\ddot{\mathbf{x}}_{P_i} = [\mathbf{a}_{P_i}^T \dot{\boldsymbol{\omega}}_{P_i}^T]^T$ (time-derivative of the twist) of point P_i: $\mathbf{a}_{P_i}$ stands for the three-component linear acceleration vector at point P_i, and $\dot{\boldsymbol{\omega}}_{P_i}$ stands for the three-component angular acceleration vector at point P_i,

and 12 outputs:

- the six components in $\mathcal{R}_i$ of the acceleration twist $\ddot{\mathbf{x}}_{C_i} = [\mathbf{a}_{C_i}^T \dot{\boldsymbol{\omega}}_{C_i}^T]^T$ of point C_i,
- the six components in $\mathcal{R}_i$ of the wrench $\mathbf{W}_{P_i} = [\mathbf{F}_{P_i}^T \mathbf{T}_{P_i}^T]^T$ applied by the link $\mathcal{L}_i$ to the substructure $\mathcal{L}_{i-1}$ at point P_i,

and can be represented by the block-diagram depicted in Fig. 3.

The way to obtain such a TITOP model $\mathbf{G}^{\mathcal{L}_i}_{P_i,C_i}(s)$ will be detailed in Sect. 3 for Euler–Bernoulli beams and is also detailed in [1] and [18] in the general case. The general procedure is based on the modal analysis of the link $\mathcal{L}_i$ with the *clamped at P_i-free at C_i* boundary

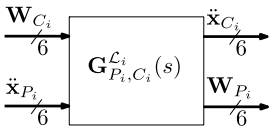


Fig. 3 Block-diagram of the TITOP model $\mathbf{G}^{\mathcal{L}_i}_{P_i,C_i}(s)$ of link $\mathcal{L}_i$

conditions. Indeed, the Lagrange formulation of dynamics using the assumed mode method (AMM) or finite element method (FEM) leads to a generalized second-order differential equation [22, 28]:

$$\begin{bmatrix} \mathbf{D}^{\mathcal{L}_i}_{P_i} & \mathbf{L}^T_{P_i} \\ \mathbf{L}_{P_i} & \mathbf{1}_{n_i} \end{bmatrix} \begin{bmatrix} \ddot{\mathbf{x}}_{P_i} \\ \ddot{\boldsymbol{\eta}}_i \end{bmatrix} + \begin{bmatrix} \mathbf{0} & \mathbf{0} \\ \mathbf{0} & \mathrm{diag}(2\xi_j\omega_j) \end{bmatrix} \begin{bmatrix} \star \\ \dot{\boldsymbol{\eta}}_i \end{bmatrix} + \begin{bmatrix} \mathbf{0} & \mathbf{0} \\ \mathbf{0} & \mathrm{diag}(\omega_j^2) \end{bmatrix} \begin{bmatrix} \star \\ \boldsymbol{\eta}_i \end{bmatrix} = \begin{bmatrix} -\mathbf{I}_6 & \boldsymbol{\tau}^T_{C_iP_i} \\ \mathbf{0} & \boldsymbol{\Phi}^T_{C_i} \end{bmatrix} \begin{bmatrix} \mathbf{W}_{P_i} \\ \mathbf{W}_{C_i} \end{bmatrix}, \tag{1}$$

where:

- n_i is the number of flexible clamped–free modes of link $\mathcal{L}_i$ characterized by the modal coordinates vector $\boldsymbol{\eta}_i$, the frequencies ω_j, $j = 1, \ldots, n_i$, and the damping ratio ξ_j, $j = 1, \ldots, n_i$,
- $\mathbf{1}_{n_i}$ is the identity matrix of size n_i,
- $\mathbf{L}_{P_i}$ is the $n_i \times 6$ modal participation factor matrix of the link at point P_i and projected in the frame $\mathcal{R}_i$,
- $\boldsymbol{\Phi}_{C_i}$ is the $6 \times n_i$ projection matrix of the n_i clamped–free modal shapes on the six d.o.f. at point C_i and projected in the frame $\mathcal{R}_i$,
- $\boldsymbol{\tau}_{C_iP_i}$ is the "rigid" kinematic model between point C_i and P_i projected in the frame $\mathcal{R}_i$: $\boldsymbol{\tau}_{C_iP_i} = \begin{bmatrix} \mathbf{1}_3 & (^*\overrightarrow{C_iP_i}) \\ \mathbf{0}_{3\times3} & \mathbf{1}_3 \end{bmatrix}$, where $(^*\overrightarrow{C_iP_i})$ is the skew-symmetric matrix associated with the vector from C_i to P_i,
- $\mathbf{D}^{\mathcal{L}_i}_{P_i}$ is the 6×6 rigid mass model of the link at point P_i and projected in the frame $\mathcal{R}_i$.

The right-hand term of Eq. (1) describes the contribution of the wrenches $\mathbf{W}_{P_i}$ and $\mathbf{W}_{C_i}$ to the generalized force vector. The acceleration twist $\ddot{\mathbf{x}}_{C_i}$ at point C_i can be easily expressed from the generalized acceleration vector, the modal shapes, and the kinematic model:

$$\text{and:} \quad \ddot{\mathbf{x}}_{C_i} = [\boldsymbol{\tau}_{C_iP_i} \quad \boldsymbol{\Phi}_{C_i}] \begin{bmatrix} \ddot{\mathbf{x}}_{P_i} \\ \ddot{\boldsymbol{\eta}}_i \end{bmatrix} \tag{2}$$

From Eqs. (1) and (2), the general state-space realization (see also the definition of a state-space realization of a given transfer in Appendix 1) of the TITOP model $\mathbf{G}^{\mathcal{L}_i}_{P_i,C_i}(s)$ reads:

$$\begin{bmatrix} \dot{\boldsymbol{\eta}}_i \\ \ddot{\boldsymbol{\eta}}_i \\ \hline \ddot{\mathbf{x}}_{C_i} \\ \mathbf{W}_{P_i} \end{bmatrix} = \left[\begin{array}{cc|cc} \mathbf{0}_{n_i\times n_i} & \mathbf{1}_{n_i} & \mathbf{0}_{n_i\times6} & \mathbf{0}_{n_i\times6} \\ -\mathrm{diag}(\omega_j^2) & -\mathrm{diag}(2\xi_j\omega_j) & \boldsymbol{\Phi}^T_{C_i} & -\mathbf{L}_{P_i} \\ \hline -\boldsymbol{\Phi}_{C_i}\mathrm{diag}(\omega_j^2) & -\boldsymbol{\Phi}_{C_i}\mathrm{diag}(2\xi_j\omega_j) & \boldsymbol{\Phi}_{C_i}\boldsymbol{\Phi}^T_{C_i} & (\boldsymbol{\tau}_{C_iP_i} - \boldsymbol{\Phi}_{C_i}\mathbf{L}_{P_i}) \\ \mathbf{L}^T_{P_i}\mathrm{diag}(\omega_j^2) & \mathbf{L}^T_{P_i}\mathrm{diag}(2\xi_i\omega_i) & (\boldsymbol{\tau}_{C_iP_i} - \boldsymbol{\Phi}_{C_i}\mathbf{L}_{P_i})^T & -\mathbf{D}^{\mathcal{L}_i}_{P_i} + \mathbf{L}^T_{P_i}\mathbf{L}_{P_i} \end{array}\right] \times \begin{bmatrix} \boldsymbol{\eta}_i \\ \dot{\boldsymbol{\eta}}_i \\ \hline \mathbf{W}_{C_i} \\ \ddot{\mathbf{x}}_{P_i} \end{bmatrix}. \tag{3}$$

This model embeds, in the same minimal state-space realization, the direct dynamic model (transfer from acceleration to force) of link i at the point P_i and the inverse dynamic model (transfer from force to acceleration) of link i at the point C_i. All data required in Eq. (3) are commonly provided by FEM software. In [18], the link between the TITOP model and substructuring methods like the Graig–Bampton decomposition and the component modes synthesis (CMS) is detailed in the general case. In [14], a custom NASTRAN/SIMULINK interface was developed to declare and manipulate the TITOP model $\mathbf{G}^{\mathcal{L}_i}_{P_i,C_i}(s)$ as a linear dynamic system object under the MATLAB/SIMULINK environment.

Let us note that the modal analysis of the left-hand term of Eq. (1) corresponds to the *free (at P_i)–free (at C_i)* case and provides six rigid modes in addition to the free–free flexible modes. These rigid modes are not taken into account in the model $\mathbf{G}^{\mathcal{L}_i}_{P_i,C_i}(s)$ defined by Eq. (3). This is one the main advantages of the TITOP model: the boundary conditions and the rigid modes can be taken into account "outside" the model. This is detailed in the following section.

2.2 Interconnection and channel inversion of TITOP models

The open-loop dynamics of the TITOP model $\mathbf{G}^{\mathcal{L}_i}_{P_i,C_i}(s)$, that is, when the inputs are null, corresponds to the link dynamics when it is clamped at P_i ($\ddot{\mathbf{x}}_{P_i} = \mathbf{0}$) and free at C_i ($\mathbf{W}_{C_i} = \mathbf{0}$). It must be noticed that all the 12 input–output channels of the model $\mathbf{G}^{\mathcal{L}_i}_{P_i,C_i}(s)$ are invertible assuming that a residual mass (inertia) of link i is attached to the points P_i and C_i along (around) the three axes. Such an assumption is valid by using the finite-element method or the assumed mode method to model the flexibility of the link.

$[\mathbf{G}^{\mathcal{L}_i}_{P_i,C_i}]^{-1_{\mathbf{I}}}(s)$ denotes the model where the channels numbered in the index vector $\mathbf{I}$ are inverted according to the procedure described in Appendix 1. This channel inversion operation is very useful to analyze the dynamics of the link $\mathcal{L}_i$ for various boundary conditions:

- clamped at P_i and clamped at C_i, using $[\mathbf{G}^{\mathcal{L}_i}_{P_i,C_i}]^{-1_{[1:6]}}(s)$ whose inputs are $\ddot{\mathbf{x}}_{C_i}$ and $\ddot{\mathbf{x}}_{P_i}$,
- free at P_i and free at C_i, using $[\mathbf{G}^{\mathcal{L}_i}_{P_i,C_i}]^{-1_{[7:12]}}(s)$ whose inputs are $\mathbf{W}_{C_i}$ and $\mathbf{W}_{P_i}$,
- free at P_i and clamped at C_i, using $[\mathbf{G}^{\mathcal{L}_i}_{P_i,C_i}]^{-1}(s)$ whose inputs are $\ddot{\mathbf{x}}_{C_i}$ and $\mathbf{W}_{P_i}$,
- or to take into account a revolute (resp. prismatic) joint at the point P_i around (resp. along) the $\mathbf{z}_i$-axis using $[\mathbf{G}^{\mathcal{L}_i}_{P_i,C_i}]^{-1_{12}}(s)$ (resp. $[\mathbf{G}^{\mathcal{L}_i}_{P_i,C_i}]^{-1_9}(s)$), that is, no torque (resp. force) can be applied by the link $\mathcal{L}_i$ to the parent substructure $\mathcal{L}_{i-1}$ around (resp. along) the $\mathbf{z}_i$-axis. A spherical joint can be taken into account using $[\mathbf{G}^{\mathcal{L}_i}_{P_i,C_i}]^{-1_{[10:12]}}(s)$.

More generally, once the TITOP model of each link is defined and the DCM $\mathbf{P}_{i/j}$ for a given nominal configuration $\boldsymbol{\theta}$ are computed, the linear model of the whole multibody system can be built by simply connecting the inputs/outputs of the TITOP models. Hereafter, some examples of interconnection are presented.

Chain-like multibody system Let us consider a flexible spacecraft $\mathcal{S}$ whose reference body frame is $(O, \mathbf{x_0}, \mathbf{y}_0, \mathbf{z}_0)$, fitted with a flexible boom $\mathcal{B}$ at point P_1 with a revolute joint along the $(P_1, \mathbf{z}_1)$-axis. The boom holds a flexible antenna $\mathcal{A}$ at point P_2. A sketch of such a multibody system is depicted in Fig. 4 (left). The block-diagram associated to this system is presented in Fig. 4 (right). It involves the three TITOP models of the three bodies with the channel inversions required by the different boundary conditions. $\mathbf{P}^a_{i/j}$ is the augmented 6×6 DCM:

$$\mathbf{P}^a_{i/j} = \begin{bmatrix} \mathbf{P}_{i/j} & \mathbf{0}_{3\times3} \\ \mathbf{0}_{3\times3} & \mathbf{P}_{i/j} \end{bmatrix}.$$

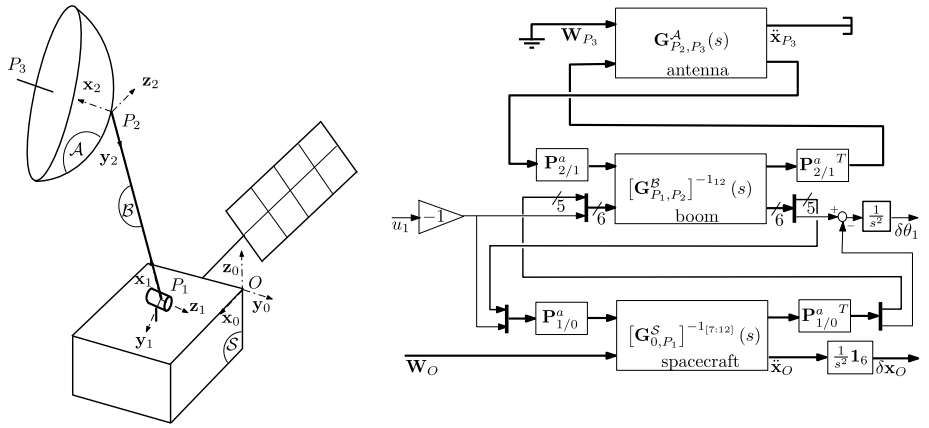


Fig. 4 A flexible boom $\mathcal{B}$ linking a flexible antenna $\mathcal{A}$ to a flexible spacecraft $\mathcal{S}$ through a revolute joint (*left*) and its block diagram model (*right*)

In this block-diagram, seven double integrators are added on the outputs to represent the seven rigid modes associated to the seven d.o.f. of this system: the six d.o.f. of the spacecraft and one d.o.f. of the revolute joint. The seven inputs of this model are the torque u_1 applied inside the revolute joint by the driven mechanism and the six components of the wrench $\mathbf{W}_0$ applied by the attitude and orbit control system at the reference point O. All dynamic couplings between the flexible modes of the antenna, the boom, and the spacecraft are directly taken into account through the feedback connections between the three TITOP models. Furthermore, the inertia j_1, the stiffness k_1, and the damping factor f_1 of the driven mechanism located in the revolute joint can be added by a feedback loop $u_1 = -j_1\ddot{\delta\theta}_1 - f_1\dot{\delta\theta}_1 - k_1\delta\theta_1$, directly plugged into the block-diagram. This can be used to handle any arbitrary boundary condition in the revolute joint, from the free condition ($j_1 = k_1 = f_1 = 0$) to the clamped condition ($k_1 \to \infty$).

Tree-like multibody system In this case, one link $\mathcal{B}$ may have two (or more) child bodies connected to $\mathcal{B}$ at points C_1 and C_2. This case is quite similar to the previous one and requires a model of the link augmented with additional ports. This case is not detailed in this paper. The reader is advised to refer to [1] where the three-port model of a link (denoted $\mathbf{G}^{\mathcal{B}}_{P,C_1,C_2}(s)$) and an example of a tree-like system are detailed (see Fig. 18 in [1]).

Closed-loop multibody system Such mechanisms are commonly modeled through the Lagrange approach using Lagrange multipliers [22, 24]. They are used to be denoted $\boldsymbol{\lambda}$ and correspond to the generalized constraint forces. Considering the model of the link $\mathcal{L}_i$ given in Eqs. (1) and (2) with a kinematic-chain closed at point C_i, the Lagrange multipliers are nothing else than the wrench at this point applied by the link $\mathcal{L}_i$: $\boldsymbol{\lambda} = -\mathbf{W}_{C_i}$. The classical Lagrange approach leads to an augmented system of differential-algebraic equations:

$$\begin{bmatrix} \mathbf{D}^{\mathcal{L}_i}_{P_i} & \mathbf{L}^T_{P_i} & \boldsymbol{\tau}^T_{C_iP_i} \\ \mathbf{L}_{P_i} & \mathbf{1}_{n_i} & \boldsymbol{\Phi}^T_{C_i} \\ \boldsymbol{\tau}_{C_iP_i} & \boldsymbol{\Phi}_{C_i} & \mathbf{0} \end{bmatrix} \begin{bmatrix} \ddot{\mathbf{x}}_{P_i} \\ \ddot{\boldsymbol{\eta}}_i \\ \boldsymbol{\lambda} \end{bmatrix} + \begin{bmatrix} \mathbf{0} & \mathbf{0} & \mathbf{0} \\ \mathbf{0} & \mathrm{diag}(2\xi_j\omega_j) & \mathbf{0} \\ \mathbf{0} & \mathbf{0} & \mathbf{0} \end{bmatrix} \begin{bmatrix} \star \\ \dot{\boldsymbol{\eta}}_i \\ \star \end{bmatrix} + \begin{bmatrix} \mathbf{0} & \mathbf{0} & \mathbf{0} \\ \mathbf{0} & \mathrm{diag}(\omega_j^2) & \mathbf{0} \\ \mathbf{0} & \mathbf{0} & \mathbf{0} \end{bmatrix} \begin{bmatrix} \star \\ \boldsymbol{\eta}_i \\ \star \end{bmatrix} = \begin{bmatrix} -\mathbf{W}_{P_i} \\ \mathbf{0} \\ \ddot{\mathbf{x}}_{C_i} \end{bmatrix}. \tag{4}$$

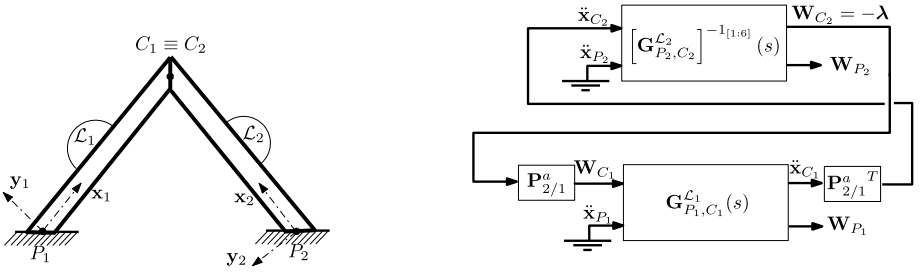


Fig. 5 A flexible closed-loop structure (*left*) and its block diagram model (*right*)

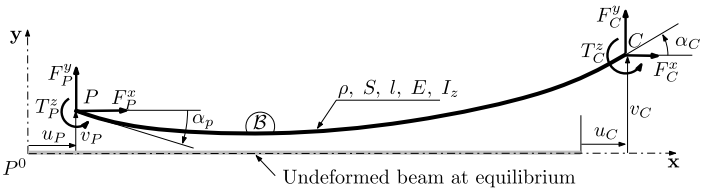


Fig. 6 A uniform beam $\mathcal{B}$ in the plane $(P^0, \mathbf{x}, \mathbf{y})$

Considering the TITOP formulation of the model in Eq. (3), $\boldsymbol{\lambda}$ (up to the sign) is an input of $\mathbf{G}^{\mathcal{L}_i}_{P_i,C_i}(s)$ or an output of the model $[\mathbf{G}^{\mathcal{L}_i}_{P_i,C_i}]^{-1_{[1:6]}}(s)$ where the upper port is inverted. Thus, the upper port of $[\mathbf{G}^{\mathcal{L}_i}_{P_i,C_i}]^{-1_{[1:6]}}(s)$ can be connected in a feedback loop to the upper port of the adjoining link in order to close the kinematic chain. Such an interconnection is presented in Fig. 5 (right) in the case of a very simple closed-loop structure composed of two links $\mathcal{L}_1$ and $\mathcal{L}_2$ clamped to the ground and one to each other at point $C_1 \equiv C_2$. In that case, the model outputs are the two wrenches $\mathbf{W}_{P_1}$ and $\mathbf{W}_{P_2}$ applied by the system to the ground at points P_1 and P_2. Similarly to the case of the chain-like multibody system example, a revolute joint around the $(C_2, \mathbf{z}_1)$-axis can be taken into account using the model $[\mathbf{G}^{\mathcal{L}_2}_{P_2,C_2}]^{-1_{[1:5]}}(s)$ to cancel the torque around this axis in the joint between $\mathcal{L}_1$ and $\mathcal{L}_2$, that is, $\boldsymbol{\lambda}(6) = \mathbf{W}_{C_i}(6) = 0$ (see also the illustration on the four-bar mechanism in Sect. 4).

3 Two-port model of a beam in the planar case

Let us consider a uniform beam $\mathcal{B}$ between points P and C, characterized by the following parameters (see Fig. 6):

- mass density ρ (kg/m^3),
- section S (m^2),
- length l (m),
- Young modulus E (N/m^2),
- second moment of area w.r.t. the $\mathbf{z}$-axis: I_z (m^4).

The objective is to compute the TITOP model $\mathbf{G}^{\mathcal{B}}_{P,C}(s)$. In the (3 d.o.f.) planar case, this model will be denoted $\mathbf{G}(s)$ and is a transfer between six inputs:

- three components F^x_C (N), F^y_C (N), and T^z_C (Nm) in the frame $\mathcal{R} = (P^0, \mathbf{x}, \mathbf{y}, \mathbf{z})$ of the planar wrench applied *to* the beam at point C,

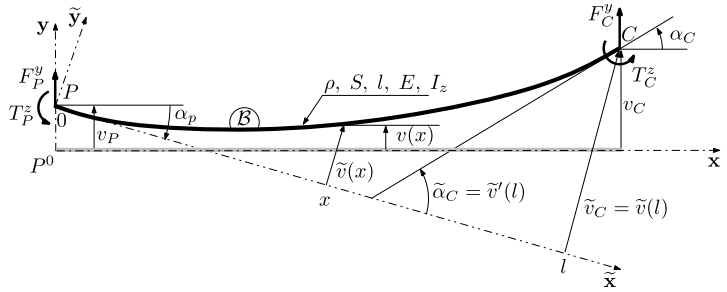


Fig. 7 Parameterization of the beam deflection at a given time t

– three components $\ddot{u}_P$ (m/s^2), $\ddot{v}_P$ (m/s^2), and $\ddot{\alpha}_P$ (rad/s^2) in the frame $\mathcal{R}$ of the planar acceleration twist of the beam at point P,

and six outputs:

– three components $\ddot{u}_C$ (m/s^2), $\ddot{v}_C$ (m/s^2), and $\ddot{\alpha}_C$ (rad/s^2) in the frame $\mathcal{R}$ of the planar acceleration twist of the beam at point C,
– three components F_P^x (N), F_P^y (N), and T_P^z (Nm) in the frame $\mathcal{R}$ of the planar wrench applied *by* the beam at point P.

This model $\mathbf{G}(s)$ is derived in following sections considering a decoupling between the pure flexion in the plane $(P^0, \mathbf{x}, \mathbf{y})$ and the pure traction–compression along the $(P^0, \mathbf{x})$-axis.

3.1 Pure flexion in the plane $(P^0, \mathbf{x}, \mathbf{y})$

A well-known approach to derive the dynamic model of a flexible beam is based on the Lagrange technique combined with the assumed modes method (AMM) [4]. This approach involves a moving body frame $\widetilde{\mathcal{R}} = (P, \tilde{\mathrm{x}}, \tilde{\mathrm{y}}, \mathrm{z})$ attached to the beam at point P (see Fig. 7). Under the small deflection assumption, the displacement $v(x,t)$ along the $\mathbf{y}$-axis at any point of abscissa x and at any time t reads as follows:

$$v(x,t) = v_P(t) + x\alpha_P(t) + \tilde{v}(x,t) \quad \forall x \in [0,l]. \tag{5}$$

The deflection $\tilde{v}(x,t)$ in the moving frame $\widetilde{\mathcal{R}}$ is split up into n shape functions $\phi_i(x)$ ($\boldsymbol{\phi}(x) = [\phi_1(x) \cdots \phi_n(x)]^T$ being the shape function vector), associated with n time-domain functions $q_i(t)$, $n = 1, \ldots, n$ ($\mathbf{q}(t) = [q_1(t) \cdots q_n(t)]^T$):

$$\tilde{v}(x,t) = \sum_{i=0}^{n} \phi_i(x) q_i(t) = \boldsymbol{\phi}(x)^T \mathbf{q}(t). \tag{6}$$

Then, the kinetic energy reads

$$\mathcal{T} = \frac{1}{2}\rho S \int_0^l \left(\dot{v}_P + x\dot{\alpha}_P + \Sigma_{i=0}^n \phi_i(x)\dot{q}_i\right)^2 dx = \frac{1}{2}\begin{bmatrix}\begin{bmatrix}\dot{v}_P \\ \dot{\alpha}_P\end{bmatrix} \\ \dot{\mathbf{q}}\end{bmatrix}^T \begin{bmatrix}\mathbf{M}_{rr} & \mathbf{M}_{rf}^T \\ \mathbf{M}_{rf} & \mathbf{M}_{ff}\end{bmatrix} \begin{bmatrix}\begin{bmatrix}\dot{v}_P \\ \dot{\alpha}_P\end{bmatrix} \\ \dot{\mathbf{q}}\end{bmatrix},$$

where:

- $\mathbf{M}_{rr} = \begin{bmatrix} \rho Sl & \frac{\rho Sl^2}{2} \\ \frac{\rho Sl^2}{2} & \frac{\rho Sl^3}{3} \end{bmatrix}$ is the 2×2 rigid mass matrix,
- $\mathbf{M}_{rf} = [\rho S \int_0^l \boldsymbol{\phi}(x)\, dx \;\; \rho S \int_0^l x\boldsymbol{\phi}(x)\, dx]$ is the $n \times 2$ rigid-flexible coupling mass matrix,
- $\mathbf{M}_{ff} = \rho S \int_0^l \boldsymbol{\phi}(x)\boldsymbol{\phi}(x)^T\, dx$ is the $n \times n$ flexible mass matrix.

The elastic potential energy reads

$$\mathcal{V} = \frac{1}{2} EI_z \int_0^l \left(\frac{\partial^2 \tilde{v}(x,t)}{\partial x^2} \right)^2 dx = \frac{1}{2} \begin{bmatrix} \begin{bmatrix} v_P \\ \alpha_P \end{bmatrix} \\ \mathbf{q} \end{bmatrix}^T \begin{bmatrix} \mathbf{0}_{2\times 2} & \mathbf{0}_{2\times n} \\ \mathbf{0}_{n\times 2} & \mathbf{K}_{n\times n} \end{bmatrix} \begin{bmatrix} \begin{bmatrix} v_P \\ \alpha_P \end{bmatrix} \\ \mathbf{q} \end{bmatrix},$$

where $\mathbf{K} = EI_z \int_0^l [\frac{d^2\boldsymbol{\phi}(x)}{dx^2}][\frac{d^2\boldsymbol{\phi}(x)}{dx^2}]^T\, dx = EI_z \int_0^l \boldsymbol{\phi}''(x)\boldsymbol{\phi}''^T(x)\, dx$ is the $n \times n$ stiffness matrix.

Applying the action–reaction principle at point P, the work of external loads is

$$W_{\text{ext}} = -v_P F_P^y - \alpha_P T_P^z + v(l) F_C^y + v'(l) T_C^z \tag{7}$$

$$= \begin{bmatrix} -v_P & -\alpha_P & v_P + l\alpha_P + \mathbf{q}^T\boldsymbol{\phi}(l) & \alpha_P + \mathbf{q}^T\boldsymbol{\phi}'(l) \end{bmatrix} \begin{bmatrix} F_P^y \\ T_P^z \\ F_C^y \\ T_C^z \end{bmatrix} \tag{8}$$

$$= \begin{bmatrix} \begin{bmatrix} v_P \\ \alpha_P \end{bmatrix} \\ \mathbf{q} \end{bmatrix}^T \begin{bmatrix} -1 & 0 & 1 & 0 \\ 0 & -1 & l & 1 \\ \mathbf{0}_{n\times 1} & \mathbf{0}_{n\times 1} & \boldsymbol{\phi}(l) & \boldsymbol{\phi}'(l) \end{bmatrix} \begin{bmatrix} F_P^y \\ T_P^z \\ F_C^y \\ T_C^z \end{bmatrix}, \tag{9}$$

and the Lagrange derivation leads to the following second-order equation:

$$\begin{bmatrix} \mathbf{M}_{rr} & \mathbf{M}_{rf}^T \\ \mathbf{M}_{rf} & \mathbf{M}_{ff} \end{bmatrix} \begin{bmatrix} \begin{bmatrix} \ddot{v}_P \\ \ddot{\alpha}_P \end{bmatrix} \\ \ddot{\mathbf{q}} \end{bmatrix} + \begin{bmatrix} \mathbf{0}_{2\times 2} & \mathbf{0}_{2\times n} \\ \mathbf{0}_{n\times 2} & \mathbf{K}_{n\times n} \end{bmatrix} \begin{bmatrix} \begin{bmatrix} v_P \\ \alpha_P \end{bmatrix} \\ \mathbf{q} \end{bmatrix} = \begin{bmatrix} -\mathbf{I}_2 & \boldsymbol{\tau}^T \\ \mathbf{0}_{n\times 2} & \boldsymbol{\Phi}^T(l) \end{bmatrix} \begin{bmatrix} \begin{bmatrix} F_P^y \\ T_P^z \end{bmatrix} \\ \begin{bmatrix} F_C^y \\ T_C^z \end{bmatrix} \end{bmatrix} \tag{10}$$

with $\boldsymbol{\tau} = \begin{bmatrix} 1 & l \\ 0 & 1 \end{bmatrix}$, the rigid kinematic model between point C and P of the beam in the planar case, and $\boldsymbol{\Phi}(l) = [\boldsymbol{\phi}(l)\; \boldsymbol{\phi}'(l)]^T$. The relation between accelerations at points C and P, under the low-speed motion assumption reads

$$\begin{bmatrix} \ddot{v}_C \\ \ddot{\alpha}_C \end{bmatrix} = \boldsymbol{\tau} \begin{bmatrix} \ddot{v}_P \\ \ddot{\alpha}_P \end{bmatrix} + \boldsymbol{\Phi}(l)\ddot{\mathbf{q}}. \tag{11}$$

From Eqs. (10) and (11) we can easily derive the state-space representation, associated with the state vector $\mathbf{x}_f = [\mathbf{q}^T\; \dot{\mathbf{q}}^T]^T$, of the TITOP model $\mathbf{G}_f(s)$ relative to the pure flexion

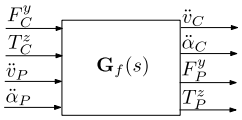


Fig. 8 TITOP model $\mathbf{G}_f(s)$ block diagram of a flexible beam in bending

dynamics in the plane $(P^0, \mathbf{x}, \mathbf{y})$ (see Fig. 8):

$$\begin{bmatrix} \dot{\mathbf{q}} \\ \ddot{\mathbf{q}} \\ \hline \begin{bmatrix} \ddot{v}_C \\ \ddot{\alpha}_C \\ F_P^y \\ T_P^z \end{bmatrix} \end{bmatrix} = \left[\begin{array}{cc|cc} \mathbf{0}_n & \mathbf{1}_n & \mathbf{0}_{n\times 2} & \mathbf{0}_{n\times 2} \\ -\mathbf{M}_{ff}^{-1}\mathbf{K} & \mathbf{0}_n & \mathbf{M}_{ff}^{-1}\boldsymbol{\Phi}^T(l) & -\mathbf{M}_{ff}^{-1}\mathbf{M}_{rf} \\ \hline -\boldsymbol{\Phi}(l)\mathbf{M}_{ff}^{-1}\mathbf{K} & \mathbf{0}_n & \boldsymbol{\Phi}(l)\mathbf{M}_{ff}^{-1}\boldsymbol{\Phi}^T(l) & \boldsymbol{\tau} - \boldsymbol{\Phi}(l)\mathbf{M}_{ff}^{-1}\mathbf{M}_{rf} \\ \mathbf{M}_{rf}^T\mathbf{M}_{ff}^{-1}\mathbf{K} & \mathbf{0}_n & (\boldsymbol{\tau} - \boldsymbol{\Phi}(l)\mathbf{M}_{ff}^{-1}\mathbf{M}_{rf})^T & \mathbf{M}_{rf}^T\mathbf{M}_{ff}^{-1}\mathbf{M}_{rf} - \mathbf{M}_{rr} \end{array}\right] \times \begin{bmatrix} \mathbf{q} \\ \dot{\mathbf{q}} \\ \hline \begin{bmatrix} F_C^y \\ T_C^z \\ \ddot{v}_P \\ \ddot{\alpha}_P \end{bmatrix} \end{bmatrix}. \tag{12}$$

3.1.1 Choice of the modal decomposition

In this section, we discuss the choice of the decomposition defined in Eq. (6) regarding the capability of the TITOP model $\mathbf{G}_f(s)$ (and its inverses) to take into account various boundary conditions. Among all possible boundary conditions, a very simple test consists in computing and comparing the natural frequencies $\omega_{cf,i}$ and $\omega_{fc,i}$ of models $\mathbf{G}_f(s)$ and $\mathbf{G}_f^{-1}(s)$, respectively. Indeed, $\mathbf{G}_f(s)$ is the model of the beam under the *clamped–free* condition and $\mathbf{G}_f^{-1}(s)$ is the model of the beam under the *free–clamped* condition. Since the beam is uniform, the natural frequencies of the two models must be equal: $\omega_{cf,i} = \omega_{fc,i}\ \forall i$.

Two decompositions are considered to build the TITOP model $\mathbf{G}_f(s)$:

- the well-known clamped–free assumed mode decomposition [12]. The model obtained from this decomposition is denoted $\mathbf{G}_{f,n}(s)$, where n is the number of assumed modes.
- the decomposition based on fifth-order polynomial shape functions [14]. The model obtained from this decomposition is denoted $\mathbf{G}_{f,\mathrm{pol}}(s)$.

Model $\mathbf{G}_{f,n}(s)$ In this case, the decomposition is based on the n first modes of the Euler–Bernoulli beam in the clamped–free condition, and the shape functions in (6) are [2, 6]

$$\phi_i(x) = \cos\beta_i x - \cosh\beta_i x - \frac{\cos\beta_i l + \cosh\beta_i l}{\sin\beta_i l + \sinh\beta_i l}(\sin\beta_i x - \sinh\beta_i x), \tag{13}$$

where β_i, $i = 1, \ldots, n$, are the n first solutions of the characteristic equation $\cos\beta l \cosh\beta l + 1 = 0$. The natural frequencies are given by $\omega_{i,\mathrm{ref}} = \beta_i^2\sqrt{\frac{EI_z}{\rho S}}$ and are the clamped–free reference values to evaluate approximate solutions. Such a decomposition basis is orthonormal and leads to $\mathbf{M}_{ff} = I_n$ and $\mathbf{K} = \mathrm{diag}([\omega_{i,\mathrm{ref}}^2])$. The values of $\mathbf{M}_{rf}$ and $\boldsymbol{\Phi}(l)$ are not detailed for brevity.

Model $\mathbf{G}_{f,\mathrm{pol}}(s)$ In this approach, given in more details in [14], the deflection $\tilde{v}(x,t)$ in the moving frame $\widetilde{\mathcal{R}}$ is expressed as

$$\tilde{v}(x,t) = a_2(t)x^2 + a_3(t)x^3 + a_4(t)x^4 + a_5(t)x^5.$$

This fifth-order polynomial ensures that $\tilde{v}(0,t) = \tilde{v}'(0,t) = 0\ \forall t$. The coefficients $a_i(t)$ are then expressed as a function of four time-domain functions $q_i(t)$ defined by

$$\mathbf{q}(t) = \begin{bmatrix} \tilde{v}''(0,t) & \tilde{v}(l,t) & \tilde{v}'(l,t) & \tilde{v}''(l,t) \end{bmatrix}^T, \tag{14}$$

and the shape functions vector reads

$$\boldsymbol{\phi}(x) = \begin{bmatrix} \frac{1}{2}x^2 - \frac{3}{2l}x^3 + \frac{3}{2l^2}x^4 - \frac{1}{2l^3}x^5 \\ \frac{10}{l^3}x^3 - \frac{15}{l^4}x^4 + \frac{6}{l^5}x^5 \\ \frac{-4}{l^2}x^3 + \frac{7}{l^3}x^4 - \frac{3}{l^4}x^5 \\ \frac{1}{2l}x^3 - \frac{1}{l^2}x^4 + \frac{1}{2l^3}x^5 \end{bmatrix}. \tag{15}$$

Data required to build the TITOP model $\mathbf{G}_{f,\mathrm{pol}}(s)$ defined in Eq. (12) are obtained using following decompositions:

$$\left[\begin{array}{c|c} \mathbf{M}_{rr} & \mathbf{M}_{rf}^T \\ \hline \mathbf{M}_{rf} & \mathbf{M}_{ff} \end{array}\right] = \frac{\rho S l}{55440} \left[\begin{array}{cc|cccc} 55440 & 27720l & 462l^2 & 27720 & -5544l & 462l^2 \\ 27720l & 18480l^2 & 198l^3 & 19800l & -3432l^2 & 264l^3 \\ \hline 462l^2 & 198l^3 & 6l^4 & 181l^2 & -52l^3 & 5l^4 \\ 27720 & 19800l & 181l^2 & 21720 & -3732l & 281l^2 \\ -5544l & -3432l^2 & -52l^3 & -3732l & 832l^2 & -69l^3 \\ 462l^2 & 264l^3 & 5l^4 & 281l^2 & -69l^3 & 6l^4 \end{array}\right], \tag{16}$$

$$\mathbf{K} = \frac{EI_z}{70l^3} \begin{bmatrix} 6l^4 & -30l^2 & 8l^3 & l^4 \\ -30l^2 & 1200 & -600l & 30l^2 \\ 8l^3 & -600l & 384l^2 & -22l^3 \\ l^4 & 30l^2 & -22l^3 & 6l^4 \end{bmatrix}, \qquad \left[\begin{array}{c} \boldsymbol{\tau}^T \\ \hline \boldsymbol{\Phi}^T(l) \end{array}\right] = \left[\begin{array}{cc} 1 & 0 \\ l & 0 \\ \hline 0 & 0 \\ 1 & 0 \\ 0 & 1 \\ 0 & 0 \end{array}\right]. \tag{17}$$

The clamped–free and free–clamped models obtained from the TITOP models $\mathbf{G}_{f,\mathrm{pol}}(s)$ and $\mathbf{G}_{f,n}(s)$ (for various numbers n of assumed modes) are now evaluated in Table 1 regarding the accuracy of the first two natural frequencies. Of course, the model $\mathbf{G}_{f,n}(s)$ provides the exact clamped–free frequencies for any values of n since the clamped–free modes are exactly taken into account in this approach. But its inverse, which must represents the free–clamped model, is not accurate at all, even for high values of n (for $n = 16$, the order of the model $\mathbf{G}_{f,16}(s)$ is 32!!). In comparison, the model $\mathbf{G}_{f,\mathrm{pol}}(s)$ is an eighth-order model with only four flexible modes, which is quite accurate regarding the first two natural frequencies from the clamped–free to free–clamped conditions.

In the following section, the TITOP model $\mathbf{G}_{f,\mathrm{pol}}(s)$ is used to model an Euler–Bernoulli beam under the various well-known boundary conditions: free, clamped, support, or sliding on each of the two tips of the beam. In each case, the first two natural frequencies are compared with the reference values provided by the beam theory.

Table 1 Comparison of the first two frequencies of TITOP models and their inverses. The direct model corresponds to the clamped–free model of an Euler–Bernoulli beam. The inverse model corresponds to the free–clamped model. Frequencies are expressed using normalized units ($\sqrt{\frac{EI_z}{\rho S l^4}}$)

i	$\omega_{i,\text{ref}}$	$\mathbf{G}_{f,\text{pol}}(s)$	$\mathbf{G}^{-1}_{f,\text{pol}}(s)$	$\mathbf{G}_{f,n}(s)$	$\mathbf{G}^{-1}_{f,4}(s)$	$\mathbf{G}^{-1}_{f,8}(s)$	$\mathbf{G}^{-1}_{f,16}(s)$
1	3.5160	3.5160	3.5160	3.5160 $\forall n$	4.4432	3.9084	3.7508
2	22.034	22.158	22.158	22.034 $\forall n$	27.486	24.579	23.585

3.1.2 Other boundary conditions

The various classical (clamped, free, pinned, sliding) boundary conditions are taken into account by setting to zero the corresponding inputs of $\mathbf{G}_{f,\text{pol}}(s)$, or of its inversion around one or more channels. The procedure for such a channel inversion is described in Appendix 1 under state-space formalism and can be directly applied to the TITOP model $\mathbf{G}_{f,\text{pol}}(s)$ defined in Eq. (12). Note that the eight-component state vector $\mathbf{x}_f$ of $\mathbf{G}_{f,\text{pol}}(s)$ or of its various inverses has a physical meaning and is defined by

$$\mathbf{x}_f = \begin{bmatrix} \mathbf{q} \\ \dot{\mathbf{q}} \end{bmatrix},$$

where more particularly (from (5) and (14))

$$\begin{aligned} \mathbf{x}_f(2) &= \mathbf{q}(2) = \tilde{v}(l) = v_C - v_P - l\alpha_P, \\ \mathbf{x}_f(3) &= \mathbf{q}(3) = \tilde{v}'(l) = \alpha_c - \alpha_P. \end{aligned} \tag{18}$$

In the various cases presented in Appendix 2, the channel inversion to be used on the TITOP model $\mathbf{G}_{f,\text{pol}}(s)$ in order to take into account the corresponding boundary conditions is detailed. Some boundary conditions can introduce also some *internal state conditions*, which can be used to reduce the order of the model. These conditions are also detailed in the various cases presented in Appendix 2. The first two natural frequencies ω_i, $i = 1, 2$, are then compared with the reference values $\omega_{i,\text{ref}}$ provided by beam theory [2] under the same boundary conditions, and the relative errors $\Delta\omega_i = 100\frac{|\omega_i - \omega_i^{\text{ref}}|}{\omega_i^{\text{ref}}}$, $i = 1, 2$, are computed and summarized in Tables 3 to 11.

Finally, we have to keep in mind that the model $\mathbf{G}_{f,\text{pol}}(s)$ and its various inverses describe the relationship between forces and accelerations. These models provide the frequencies of the flexible modes for various boundary conditions. To take into account the rigid modes that can appear in some cases (free–free, pinned–free, sliding–free, sliding–sliding), we have to consider the positions v_P, α_P, v_C, and α_C as outputs of an augmented model. Of course, these positions can be obtained from accelerations using twice integrations, but it is recommended to use the internal state $\mathbf{x}_f$ and Eqs. (18) to describe this augmented model by a minimal state-space representation. The block-diagram representation of this augmented model and the number of rigid modes are also detailed for the various cases presented in Appendix 2.

In every case, the TITOP model $\mathbf{G}_{f,\text{pol}}(s)$ and its inverses provide a quite good approximation of the first two natural frequencies.

In conclusion, the polynomial approximation done in the TITOP model $\mathbf{G}_{f,\text{pol}}(s)$ leads to a simple analytical model (order 8), which can be used during preliminary design phase.

It allows varying conditions on a very large range, from clamped to free conditions, for each translational or rotational d.o.f. The fifth-order polynomial shape functions chosen to build the TITOP model allow the first two natural frequencies to be representative enough for arbitrary boundary conditions. The only task needed to vary these boundary conditions consists of the inversion of input/output channels of the TITOP model or the feedback of some dynamic model between its input and output ports. That will be illustrated in Sect. 4.

3.1.3 Modal shapes of TITOP models

Let us consider the eighth-order TITOP model of the beam $\mathbf{G}_{f,\text{pol}}(s)$ or its inverses $\mathbf{G}_{f,\text{pol}}^{-1\mathbf{I}}(s)$. For all these models, the state vector is still $\mathbf{x}_f(t) = [\mathbf{q}^T(t) \quad \dot{\mathbf{q}}^T(t)]^T$.

Let $\mathbf{A}$, $\mathbf{B}$, $\mathbf{C}$, and $\mathbf{D}$ be the four state-space matrices of one of these models. Then the eigenvalue decomposition of $\mathbf{A}$ characterizes the free response of the model to initial conditions $\mathbf{x}_f(0)$ (i.e., when the inputs are set to 0). The eigenvalues λ_i of $\mathbf{A}$ are auto-conjugate pairs associated with each natural frequency ($\lambda_i = \pm j\omega_i$) of the ith flexible mode ($i = 1, \ldots, 4$). The associated eigenvector $\mathbf{v}_i$ represents the magnitude of the ith mode on the components of the state vector $\mathbf{x}_f$:

$$\mathbf{x}_f(t) = \begin{bmatrix} \mathbf{q}(t) \\ \dot{\mathbf{q}}(t) \end{bmatrix} = \sum_{i=1}^{4} g_i \mathbf{v}_i e^{j(\omega_i t + \varphi_i)}, \tag{19}$$

where the scalars g_i and φ_i depend on the initial conditions $\mathbf{x}_f(0)$.

From Eqs. (5) and (6), the deformation of the beam is

$$v(x,t) = \begin{bmatrix} 1 & x & \boldsymbol{\phi}^T(x) \end{bmatrix} \begin{bmatrix} v_P(t) \\ \alpha_P(t) \\ \mathbf{q}(t) \end{bmatrix},$$

where $\boldsymbol{\phi}(x)$ is defined by (15).

Modal shapes can be characterized by their contributions to the second time-derivative of the beam deflection $\ddot{v}(x,t)$ (which is proportional to a factor $-\omega_i^2$ to the beam deflection $v(x,t)$). Indeed, let $\psi_i(x)$ be the modal shape of the ith mode; then $v(x,t)$ can be decomposed as

$$v(x,t) = \sum_{i=1}^{4} g_i \psi_i(x) e^{j(\omega_i t + \varphi_i)}$$

and

$$\ddot{v}(x,t) = -\sum_{i=1}^{4} g_i \omega_i^2 \psi_i(x) e^{j(\omega_i t + \varphi_i)} = \begin{bmatrix} 1 & x & \boldsymbol{\phi}^T(x) \end{bmatrix} \begin{bmatrix} \ddot{v}_P(t) \\ \ddot{\alpha}_P(t) \\ \ddot{\mathbf{q}}(t) \end{bmatrix}. \tag{20}$$

$\ddot{\mathbf{q}}(t)$ can be decomposed using (19) and the state matrix $\mathbf{A}$ (see Appendix 1 for the submatrix notation):

$$\ddot{\mathbf{q}}(t) = \sum_{i=1}^{4} g_i \mathbf{A}([5:8],:)\mathbf{v}_i e^{j(\omega_i t + \varphi_i)} = -\sum_{i=1}^{4} g_i \omega_i^2 \mathbf{v}_i([1:4]) e^{j(\omega_i t + \varphi_i)}. \tag{21}$$

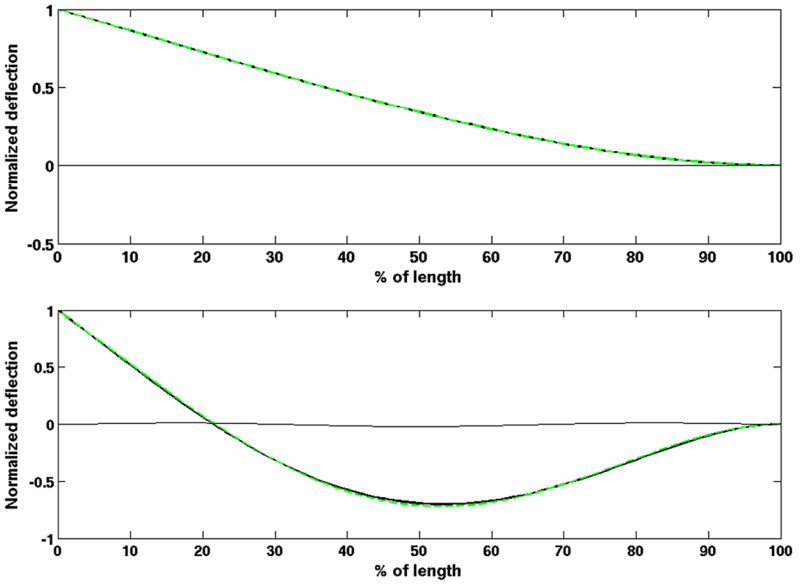


Fig. 9 Modal shapes of the first (*top*) and second (*bottom*) free–clamped modes: $\psi_i(x)$ (*solid bold*), reference $\phi_i(x)$ (*dashed*), and error $\phi_i(x) - \psi_i(x)$ (*solid*)

If the beam is clamped at P, then $\ddot{v}_P(t) = \ddot{\alpha}_P(t) = 0$, and the identification of Eq. (20) with (21) gives

$$\psi_i(x) = -\boldsymbol{\phi}^T(x)\mathbf{A}\big([5:8],:\big)\mathbf{v}_i/\omega_i^2 = \boldsymbol{\phi}^T(x)\mathbf{v}_i\big([1:4]\big).$$

In the other cases, according to the channels (defined in the vector of indexes $\mathbf{I}$) which are inverted in the model $\mathbf{G}_{f,\mathrm{pol}}^{-1_\mathbf{I}}(s)$, $\ddot{v}_P(t)$ and $\ddot{\alpha}_P(t)$ can be outputs in the model, and their contribution to the modal shape $\psi_i(x)$ can be characterized using the matrix $\mathbf{C}$ of the model state-space representation. In a general way, we can define:

$$\mathbf{C}_{v_P} = \mathbf{C}(3,:) \quad \text{if} \quad 3 \in \mathbf{I}, \quad \mathbf{C}_{v_P} = \mathbf{0}_{1\times 8} \quad \text{otherwise},$$
$$\mathbf{C}_{\alpha_P} = \mathbf{C}(4,:) \quad \text{if} \quad 4 \in \mathbf{I}, \quad \mathbf{C}_{\alpha_P} = \mathbf{0}_{1\times 8} \quad \text{otherwise}.$$

Then,

$$\psi_i(x) = -\begin{bmatrix}1 & x & \boldsymbol{\phi}^T(x)\end{bmatrix}\begin{bmatrix}\mathbf{C}_{v_P}\\ \mathbf{C}_{\alpha_P}\\ \mathbf{A}([5:8],:)\end{bmatrix}\mathbf{v}_i/\omega_i^2. \tag{22}$$

Thus, the modal shapes for arbitrary boundary conditions can be easily characterized from the eigenvectors/eigenvalues decomposition of the TITOP model or its inverses. As an example, the modal shapes $\psi_1(x)$ and $\psi_2(x)$ of the first two modes of the free–clamped beam modeled by $\mathbf{G}_{f,\mathrm{pol}}^{-1_{[1:4]}}(s)$ are depicted in Fig. 9 and compared with the reference modal shapes $\phi_1(x)$ and $\phi_2(x)$ provided by Eq. (13) by changing x by $l - x$. We can appreciate the accuracy of the first two modal shapes provided by the TITOP model.

3.2 Pure traction along $(P^0, \mathbf{x})$-axis

Only one flexible mode is considered to represent the traction–compression along the $(P^0, \mathbf{x})$-axis. Let $u(x,t)$ be the axial deformation at any point of abscissa x ($x \in [0; l]$) due to axial forces $-F_P^x$ and F_C^x applied to the beam at points P and C, respectively. Then, we assume that

$$u(x,t) = u_P(t) + \frac{x}{l}\big(u_C(t) - u_P(t)\big) = u_P(t) + \frac{x}{l}\delta_u(t) = \begin{bmatrix} 1 & \frac{x}{l} \end{bmatrix} \begin{bmatrix} u_P(t) \\ \delta_u(t) \end{bmatrix},$$

that is, the deformation at x is proportional to the total deformation $\delta_u(t)$ of the beam.

Then, the kinetic energy reads

$$\mathcal{T}_x = \frac{1}{2}\int_0^l \rho S \left(\frac{\partial u}{\partial t}(x,t)\right)^2 dx = \frac{1}{2}[\dot{u}_P \quad \dot{\delta}_u]\mathbf{M}_x \begin{bmatrix} \dot{u}_P \\ \dot{\delta}_u \end{bmatrix}$$

with $\mathbf{M}_x = \rho S l \begin{bmatrix} 1 & 1/2 \\ 1/2 & 1/3 \end{bmatrix}$, and the potential energy reads

$$\mathcal{V}_x = \frac{1}{2}\int_0^l ES \left(\frac{\partial u}{\partial x}(x,t)\right)^2 dx = \frac{1}{2}[u_p \quad \delta_u]\mathbf{K}_x \begin{bmatrix} u_p \\ \delta_u \end{bmatrix}$$

with $\mathbf{K}_x = \frac{ES}{l}\begin{bmatrix} 0 & 0 \\ 0 & 1 \end{bmatrix}$.

The TITOP model $\mathbf{G}_t(s)$ relative to the traction/compression dynamics along the $(P^0, \mathbf{x})$-axis is

$$\begin{bmatrix} \dot{\delta}_u \\ \ddot{\delta}_u \\ \hline \ddot{u}_C \\ F_P^x \end{bmatrix} = \left[\begin{array}{cc|cc} 0 & 1 & 0 & 0 \\ -\frac{3E}{\rho l^2} & 0 & \frac{3}{\rho S l} & -\frac{3}{2} \\ \hline -\frac{3E}{\rho l^2} & 0 & \frac{3}{\rho S l} & -\frac{1}{2} \\ \frac{3ES}{2l} & 0 & -\frac{1}{2} & -\frac{\rho S l}{4} \end{array}\right] \begin{bmatrix} \delta_u \\ \dot{\delta}_u \\ \hline F_C^x \\ \ddot{u}_P \end{bmatrix}. \tag{23}$$

3.3 Two-port model $\mathbf{G}(s)$ of a beam in the planar case

From Eqs. (12) and (23), the 6×6 tenth-order TITOP model $\mathbf{G}(s)$ of the beam in the plane $(P^0, \mathbf{x}, \mathbf{y})$ reads

$$\mathbf{G}(s) = \mathbf{T}\begin{bmatrix} \mathbf{G}_f(s) & \mathbf{0}_{4\times 2} \\ \mathbf{0}_{2\times 4} & \mathbf{G}_t(s) \end{bmatrix}\mathbf{T}^T, \tag{24}$$

where the permutation matrix $\mathbf{T}$ is

$$\mathbf{T} = \begin{bmatrix} 0 & 0 & 0 & 1 & 0 & 0 \\ 1 & 0 & 0 & 0 & 0 & 0 \\ 0 & 1 & 0 & 0 & 0 & 0 \\ 0 & 0 & 0 & 0 & 0 & 1 \\ 0 & 0 & 1 & 0 & 0 & 0 \\ 0 & 0 & 0 & 1 & 0 & 0 \end{bmatrix}.$$

The block-diagram of $\mathbf{G}(s)$ is depicted in Fig. 10.

In [14], the TITOP model of a uniform beam in detailed in the three-dimensional case. This parametric model is then used to model and design a boom linking a flexible deployable antenna to a flexible spacecraft.

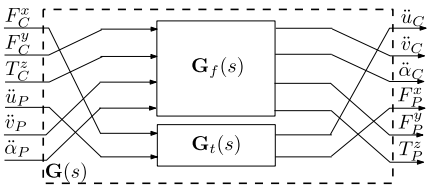


Fig. 10 TITOP model $\mathbf{G}(s)$ block diagram

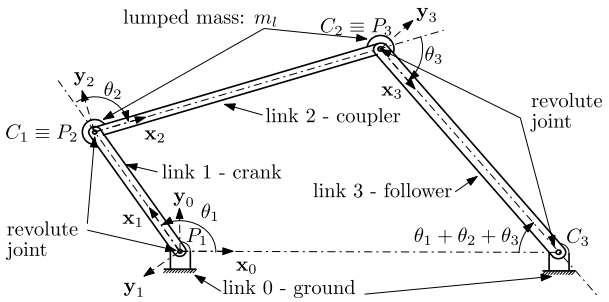


Fig. 11 Four-bar mechanism

Table 2 Four-bar mechanism links properties

i	0	1	2	3
Name	ground	crank	coupler	follower
Length l_i (m)	0.254	0.108	0.2794	0.2705
Cross section S_i (m^2)	–	1.0774×10^{-4}	4.0645×10^{-5}	4.0645×10^{-5}
Flexural rigidity $(EI)_i$ (Nm^2)	–	11.472	0.616	0.616

Each link is a uniform beam with mass density $\rho = 2714$ Kg/m^3 and modulus of elasticity $E = 7.110^{10}$ N/m^2. The lumped masses of bearing assemblies in revolute joints between link 2 and link 3 and between link 3 and link 4 are equal: $m_l = 0.042$ kg

4 Illustration: planar flexible four-bar mechanism

In this section, the two-input–two-output model approach presented in the previous section is applied to the well-known four-bar mechanism depicted in Fig. 11, taking into account the flexibility in the crank, in the coupler, and in the follower. This mechanism is a closed-loop kinematic chain with one rigid degree-of-freedom and was largely studied in the past decades [9, 23, 29] and more recently [25] to design an efficient vibrating actuator. The objective is to compute the linear model $\mathbf{G}_{4\,\text{bars}}(s, \theta_1)$ between the torque $T_{P_1}^z$ applied on the crank at point P_1 and the angular acceleration of the crank $\ddot{\alpha}_{P_1} = \delta\ddot{\theta}_1$ for a given angular configuration θ_1. First natural frequencies and modal shapes of the mechanism are then analyzed with respect to the crank angle θ_1. The numerical values are taken from [9] (translated in the International System of Units) for result comparison and summarized in Table 2. The corresponding natural frequencies are then called free frequencies (and denoted $\omega_f(i)$) since the crank is free to rotate around the $(P_1, \mathbf{z}_1)$ axis. The modeling approach provides also the cantilevered frequencies $\omega_c(i)$, thats is, when the crank is clamped on the ground, which are easily computed by considering the inverse model $\mathbf{G}_{4\,\text{bars}}^{-1}(s, \theta_1)$.

From data of Table 2, TITOP models of the crank $\mathbf{G}_1(s)$, the coupler $\mathbf{G}_2(s)$, and the follower $\mathbf{G}_3(s)$ can be built from Eqs. (12), (16), (17), (23), and (24). The ground ($i = 0$

or 4) is assumed to be rigid. The planar wrenches and acceleration twists on the inputs and outputs of each model $\mathbf{G}_i(s)$ are expressed in the body frame $\mathcal{R}_i$. Considering the linear model around a given angular configuration (small variations), all the frames $\mathcal{R}_i$ are assumed to be inertial frames. For a given crank angle θ_1, two kinematic constraints hold:

$$l_1 \cos\theta_1 + l_2 \cos(\theta_1 + \theta_2) + l_3 \cos(\theta_1 + \theta_2 + \theta_3) = l_0,$$
$$l_1 \sin\theta_1 + l_2 \sin(\theta_1 + \theta_2) + l_3 \sin(\theta_1 + \theta_2 + \theta_3) = 0.$$

They are solved in θ_2 and θ_3 using the equations given by Shigley and Uicker [23]. The values of θ_i, $i = 1, 2, 3$, allow the (planar) direction cosine matrices between the various frames $\mathcal{R}_i$ to be computed:

$$\mathbf{P}_{i/i-1} = \begin{bmatrix} \cos\theta_i & -\sin\theta_i \\ \sin\theta_i & \cos\theta_i \end{bmatrix}.$$

The revolute joints between the links enforce geometrical constraints between inputs and outputs of models $\mathbf{G}_i(s)$:

$$P_i \equiv C_{i-1} \quad \Rightarrow \quad \begin{bmatrix} \ddot{u}_{P_i} \\ \ddot{v}_{P_i} \end{bmatrix} = \mathbf{P}^T_{i/i-1} \begin{bmatrix} \ddot{u}_{C_{i-1}} \\ \ddot{v}_{C_{i-1}} \end{bmatrix}.$$

Some dynamic boundary conditions also hold on the inputs of the three models using channel(s) inversion if required:

– for the crank ($i = 1$) and the coupler ($i = 2$), the inputs of the model i must take into account that: (i) $F^x_{C_i}$ and $F^y_{C_i}$ are constrained by the contact force applied by link $i + 1$ and the inertial force of the lumped mass:

$$\begin{bmatrix} F^x_{C_i} \\ F^y_{C_i} \end{bmatrix} = \mathbf{P}_{i+1/i} \begin{bmatrix} F^x_{P_{i+1}} \\ F^y_{P_{i+1}} \end{bmatrix} - m_l \begin{bmatrix} \ddot{u}_{C_i} \\ \ddot{v}_{C_i} \end{bmatrix}, \tag{25}$$

(ii) $T^z_{C_i} = 0$ due to the revolute joint (no torque can be applied though the passive revolute joint), (iii) $-T^z_{P_i}$ is equal to the torque u applied by the driven system (crank case) or $T^z_{P_i} = 0$ if the revolute joint is free (coupler case). Thus, $T^z_{P_i}$ must be on the input, and the models to be used for the crank and the coupler are $\mathbf{G}_1^{-1_6}(s)$ and $\mathbf{G}_2^{-1_6}(s)$, respectively,

– for the follower ($i = 3$), the same condition on $T^z_{P_3}$ appears, but it is necessary to invert the first two channels of $\mathbf{G}_3(s)$ in order to close the kinematic loop, and to impose that $\ddot{u}_{C_3}$ and $\ddot{v}_{C_3}$ are zero due to the revolute joint on ground. Then, the model to be used for the follower is $\mathbf{G}_3^{-1_{[1,2,6]}}(s)$ and the first two outputs are the forces $F^x_{C_3}$ and $F^y_{C_3}$ applied by the follower on the ground.

All these geometrical and dynamical boundary conditions can be easily expressed using the block diagram model depicted in Fig. 12. From this block diagram representation, the model $\mathbf{G}_{4\,\text{bars}}(s, \theta_1)$ between the torque u applied to the crank and the crank acceleration $y = \ddot{\alpha}_{P_1}$ can then be easily derived using MATLAB/SIMULINK and the function `linmod`. The modal analysis of this model provides the free pulsations $\omega_f(i)$ of the mechanism. Note that the order of $\mathbf{G}_{4\,\text{bars}}(s, \theta_1)$ is 30: this model includes 15 flexible modes (five modes per link with four modes for bending in the plane $(P_i, \mathbf{y}_i, \mathbf{z}_i)$ and one mode for traction–compression along the $(P_i, \mathbf{x}_i)$-axis). But this model does not include the rigid mode of the mechanism.

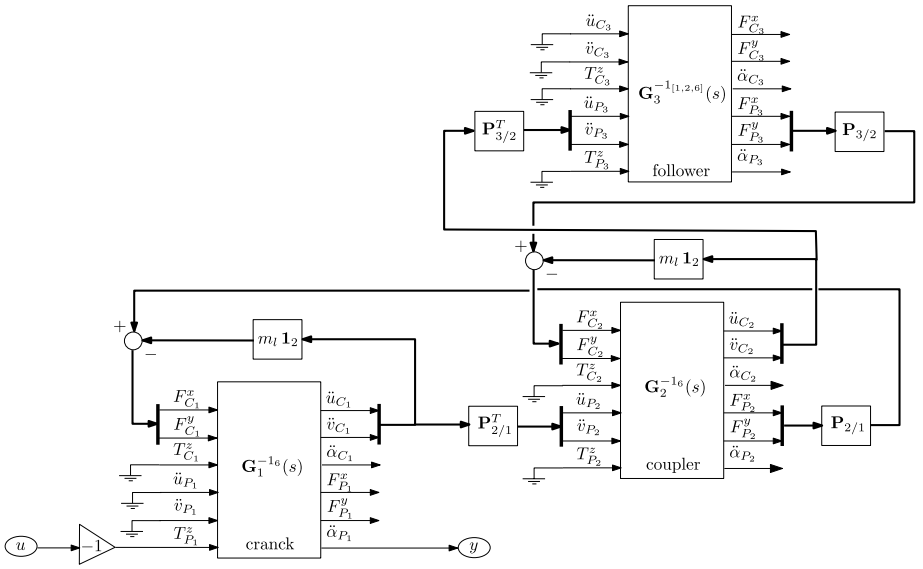


Fig. 12 Block-diagram of model $\mathbf{G}_{4\,\text{bars}}(s,\theta_1)$ between the crank torque u and the crank acceleration $y=\ddot{\alpha}_{P_1}$

For control design purpose, this rigid mode can be included augmenting the model by a double integration:

$$\frac{\alpha_{p_1}}{u}(s,\theta_1)=\mathbf{G}_{4\,\text{bars}}(s,\theta_1)\frac{1}{s^2}.$$

To evaluate the accuracy of this model, the cantilevered pulsations $\omega_c(i)$ are computed from the inverse model $\mathbf{G}_{4\,\text{bars}}^{-1}(s,\theta_1)$ and compared with the results already published on the same mechanism [9], [29]. The first, second, and third cantilevered frequencies are plotted in Fig. 13 versus crank angle. The modal shapes of the mechanism computed from the accelerations (see Sect. 3.1.3) of the first three modes for two crank angle configurations (0 and 180°) are plotted in Figs. 14 and 15. We can see that these results fit exactly the ones presented in [9].

5 Conclusions

The objective of this paper is to present the interest of the two-input–two-output port approach to model any kind of flexible multibody systems. The novelty lies in the manipulation of transfer between accelerations and forces and to embed, in the same minimal state-space representation, the direct dynamic model of a body seen from one point and the inverse dynamic model seen from another point. All channels of this transfer are invertible allowing us to consider arbitrary boundary conditions at these points. By comparison with the Newton–Euler method, commonly used to model multibody system dynamics, the forward and backward recursions are directly solved by the feedback connections between the inputs and the outputs of the TITOP models of each body. Such a dynamic model is today restricted to the linear behavior of the multibody system and to loads lumped at some particular points

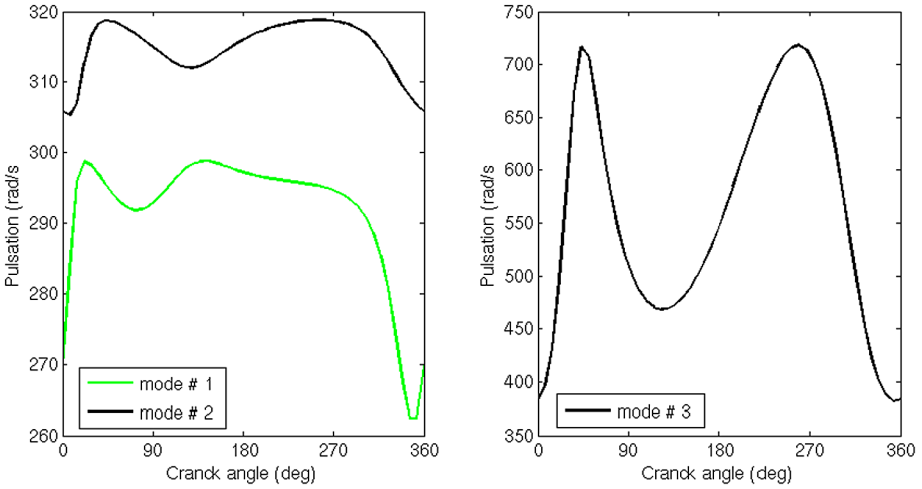


Fig. 13 $\omega_c(i)$, $i = 1, 2, 3$, versus crank angle θ_1

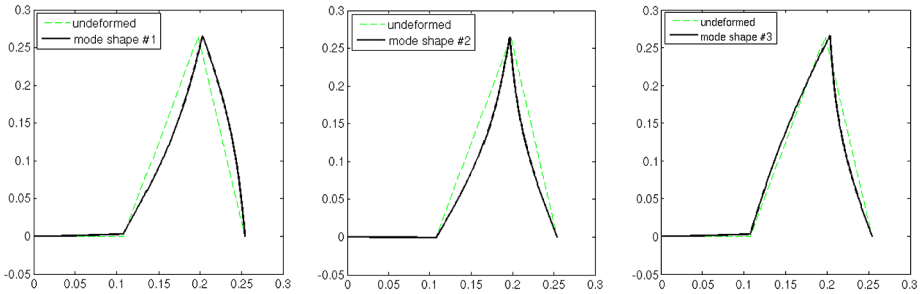


Fig. 14 First three modal shapes for crank angle $\theta_1 = 0$

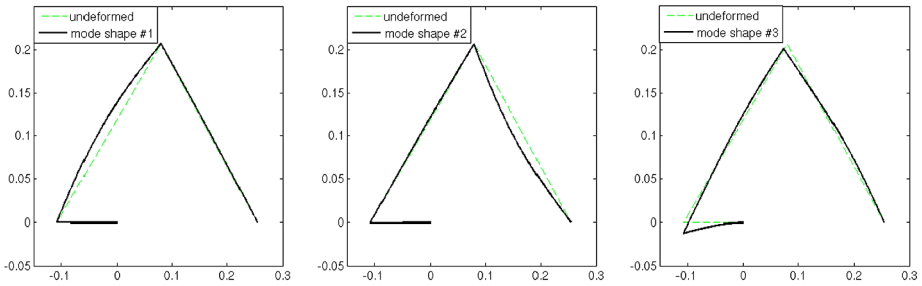


Fig. 15 First three modal shapes for crank angle $\theta_1 = 180$ deg

of the structure. The methodological utility of this approach has been highlighted on the flexible four-bar mechanism.

Further works need to be performed to extend this approach to aeronautical engineering and, more particularly, to take into account distributed loads along each body of the system and nonlinear effects, which could appear when the rate of variation of the configuration

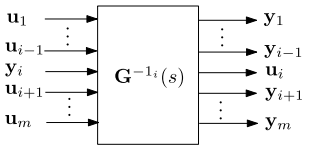


Fig. 16 Inversion of the ith channel of $\mathbf{G}$

parameters is determinant. In this current state, this approach is fully applicable to space applications (large flexible orbital structures), but the proposed extensions are still required to apply it, for instance, to the helicopter rotor dynamic model.

Acknowledgements This research is supported, in part, by ONERA (The French Aerospace Lab), CNES (The French Space Agency), ESA (European Space Agency), Thales Alenia Space and Polytechnique Montréal. We would like to thank more particularly Christelle Cumer, Thomas Loquen, Christelle Pittet, Finn Ankersen, Luca Massotti, Catherine le Peuvédic, Chiara Toglia, David-Alexandre Saussié, and Hari Murali.

Appendix 1: Matrix and linear system operations

In this section, we present basic operations on matrices and linear dynamic systems and finally the inversion of one (or more) input–output channel(s) in a linear system.

Let us consider a square (the same number of inputs and outputs) linear system $\mathbf{G}(s)$ (s stands for the Laplace variable) with order n and m channels (i.e., m inputs and m outputs). A state-space realization of the system $\mathbf{G}(s)$ is a set of four matrices $\mathbf{A}_{n\times n}$, $\mathbf{B}_{n\times m}$, $\mathbf{C}_{m\times n}$, and $\mathbf{D}_{m\times m}$ such that

$$\mathbf{G}(s) = \mathbf{D} + \mathbf{C}(s\mathbf{I}_n - \mathbf{A})^{-1}\mathbf{B}, \quad \text{also noted:} \quad \mathbf{G}(s) \equiv \left[\begin{array}{c|c} \mathbf{A} & \mathbf{B} \\ \hline \mathbf{C} & \mathbf{D} \end{array}\right]. \tag{26}$$

Submatrices and subsystems MATLAB nomenclature is used to define the submatrix $\mathbf{M}(\mathbf{I}, \mathbf{J})$ (resp. subsystem $\mathbf{G}_{\mathbf{I},\mathbf{J}}(s)$) restricted to the rows (resp. outputs) and the columns (resp. inputs) ordered in vectors of indices $\mathbf{I}$ and $\mathbf{J}$.

Single-channel inversion The system corresponding to the inversion of the ith channel of the system $\mathbf{G}(s)$ ($i \in [1, m]$) is denoted $\mathbf{G}^{-1_i}(s)$ and can be characterized by the following state-space realization (Eq. (27)).

Let $\mathbf{J}$ be the vector of indices form 1 to m without i: $\mathbf{J} = [1, \ldots, i-1, i+1, \ldots, m]$. Assume that $\mathbf{D}(i,i) \neq 0$. Then let us denote $f_i = \frac{1}{\mathbf{D}(i,i)}$ and define

$$\widetilde{\mathbf{G}}^{-1_i}(s) \equiv \left[\begin{array}{c|cc} \mathbf{A} - f_i\mathbf{B}(:,i)\mathbf{C}(i,:) & [\mathbf{B}(:,\mathbf{J}) - f_i\mathbf{B}(:,i)\mathbf{D}(i,\mathbf{J}) & f_i\mathbf{B}(:,i)] \\ \hline \left[\begin{array}{c} \mathbf{C}(\mathbf{J},:) - f_i\mathbf{D}(\mathbf{J},i)\mathbf{C}(i,:) \\ -f_i\mathbf{C}(i,:) \end{array}\right] & \left[\begin{array}{cc} \mathbf{D}(\mathbf{J},\mathbf{J}) - f_i\mathbf{D}(\mathbf{J},i)\mathbf{D}(i,\mathbf{J}) & f_i\mathbf{D}(\mathbf{J},i) \\ -f_i\mathbf{D}(i,\mathbf{J}) & f_i \end{array}\right] \end{array}\right].$$

In $\widetilde{\mathbf{G}}^{-1_i}(s)$, the ith inverted channel appears on the last channel; it is thus required to reorder the channels using the vector of indices $\mathbf{K} = [1, \ldots, i-1, m, i+1, \ldots, m-1]$, and then

$$\mathbf{G}^{-1_i}(s) = \widetilde{\mathbf{G}}^{-1_i}_{\mathbf{K},\mathbf{K}}(s). \tag{27}$$

Let $\mathbf{u}$ and $\mathbf{y}$ be the input and output vectors of $\mathbf{G}$. This inversion can be represented by the block diagram depicted in Fig. 16.

Multichannel inversion Let $\mathbf{I}$ be the vector (with q components) of indices corresponding to the channels to be inverted. The successive inversion of the q channels in $\mathbf{G}(s)$ is denoted

$$\mathbf{G}^{-1_{\mathbf{I}}}(s) = \left[\left[\left[\mathbf{G}^{-1_{\mathbf{I}(1)}}\right]^{-1_{\mathbf{I}(2)}}\right]^{\cdots}\right]^{-1_{\mathbf{I}(q)}}(s). \tag{28}$$

Appendix 2: TITOP model of the EULER–BERNOULLI beam under various boundary conditions

Case 1: free–free beam (Fig. 17) The model $\mathbf{G}^{-1_{[3,4]}}_{f,\text{pol}}(s)$ is used to set to zero its inputs F_c^y, T_c^z, F_P^y, and T_P^z. The augmented model with the two rigid modes is depicted in Fig. 17 (right).

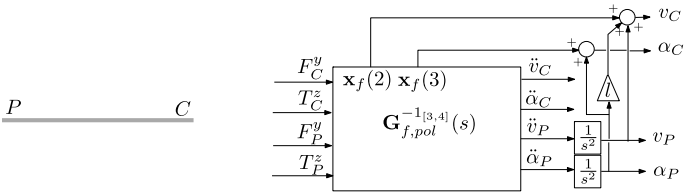


Fig. 17 The free–free beam (*left*) and its block-diagram model (*right*)

Table 3 The first two natural frequencies ω_i of the free–free beam model $\mathbf{G}^{-1_{[3,4]}}_{f,\text{pol}}(s)$ and the relative errors with the reference values $\omega_{i,\text{ref}}$

i	$\omega_{i,\text{ref}}(\sqrt{\frac{EI_z}{\rho Sl^4}})$	$\omega_i(\sqrt{\frac{EI_z}{\rho Sl^4}})$	$\Delta\omega_i$ (%)
1	22.373	22.564	0.85
2	61.673	63.537	3.0

Case 2: clamped–clamped beam (Fig. 18) The model $\mathbf{G}^{-1_{[1,2]}}_{f,\text{pol}}(s)$ is used to set to zero its inputs $\ddot{v}_C$, $\ddot{\alpha}_C$, $\ddot{v}_P$, and $\ddot{\alpha}_P$. There are no rigid modes in this case. The internal state constraints

$$\tilde{v}(l) = \mathbf{x}_f(2) = 0, \tilde{v}'(l) = \mathbf{x}_f(3) = 0\ \forall t \Rightarrow \dot{\mathbf{x}}_f(2) = \dot{\mathbf{x}}_f(3) = \dot{\mathbf{x}}_f(6) = \dot{\mathbf{x}}_f(7) = 0$$

can be used to truncate the state-space representation of $\mathbf{G}^{-1_{[1,2]}}_{f,\text{pol}}(s)$ to a fourth-order model. The frequencies of the two flexible modes are displayed in Table 4.

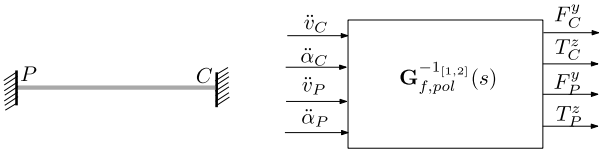


Fig. 18 The clamped–clamped beam (*left*) and its block-diagram model (*right*)

Table 4 The first two natural frequencies ω_i of the clamped–clamped beam model $\mathbf{G}^{-1_{[1,2]}}_{f,\text{pol}}(s)$ and the relative errors with the reference values $\omega_{i,\text{ref}}$

i	$\omega_{i,\text{ref}}(\sqrt{\frac{EI_z}{\rho Sl^4}})$	$\omega_i(\sqrt{\frac{EI_z}{\rho Sl^4}})$	$\Delta\omega_i$ (%)
1	22.373	22.45	0.34
2	61.673	62.929	2.0

Case 3: pinned–free beam (Fig. 19) The model $\mathbf{G}_{f,\text{pol}}^{-1_4}(s)$ is used to set to zero its inputs F_C^y, T_C^z, $\ddot{v}_P$, and T_P^z. The augmented model with the rigid mode is depicted in Fig. 19 (right).

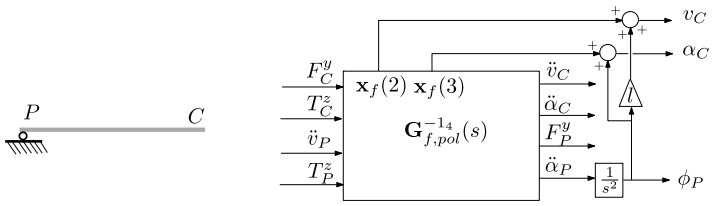


Fig. 19 The pinned–free beam (*left*) and its block-diagram model (*right*)

Table 5 The first two natural frequencies ω_i of the pinned–free beam model $\mathbf{G}_{f,\text{pol}}^{-1_4}(s)$ and the relative errors with the reference values $\omega_{i,\text{ref}}$

i	$\omega_{i,\text{ref}}(\sqrt{\frac{EI_z}{\rho Sl^4}})$	$\omega_i(\sqrt{\frac{EI_z}{\rho Sl^4}})$	$\Delta\omega_i$ (%)
1	15.418	15.445	0.17
2	49.965	51.206	2.5

Case 4: pinned–clamped beam (see Fig. 20) The model $\mathbf{G}_{f,\text{pol}}^{-1_{[1,2,4]}}(s)$ is used to set to zero its inputs $\ddot{v}_C$, $\ddot{\alpha}_C$, $\ddot{v}_P$, and T_P^z. There are no rigid modes in this case. The internal state constraints

$$\tilde{v}(l) - l\tilde{v}'(l) = \mathbf{x}_f(2) - l\mathbf{x}_f(3) = 0 \;\forall t \Rightarrow \dot{\mathbf{x}}_f(2) - l\dot{\mathbf{x}}_f(3) = \dot{\mathbf{x}}_f(6) - l\dot{\mathbf{x}}_f(7) = 0$$

can be used to reduce the state-space representation of $\mathbf{G}_{f,\text{pol}}^{-1_{[1,2,4]}}(s)$ to a sixth-order model.

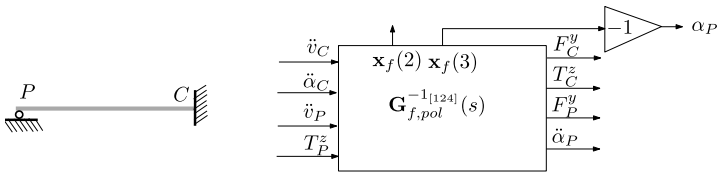


Fig. 20 The pinned–clamped beam (*right*) and its block-diagram model (*left*)

Table 6 The first two natural frequencies ω_i of the pinned–clamped beam model $\mathbf{G}_{f,\text{pol}}^{-1_{[1,2,4]}}(s)$ and the relative errors with the reference values $\omega_{i,\text{ref}}$

i	$\omega_{i,\text{ref}}(\sqrt{\frac{EI_z}{\rho Sl^4}})$	$\omega_i(\sqrt{\frac{EI_z}{\rho Sl^4}})$	$\Delta\omega_i$ (%)
1	15.418	15.433	0.1
2	49.965	50.724	1.5

Case 5: pinned–pinned beam (Fig. 21) The model $\mathbf{G}_{f,\text{pol}}^{-1_{[1,4]}}(s)$ is used to set to 0 its inputs: $\ddot{v}_C$, T_c^z, $\ddot{v}_P$, and T_P^z. There are no rigid modes in this case.

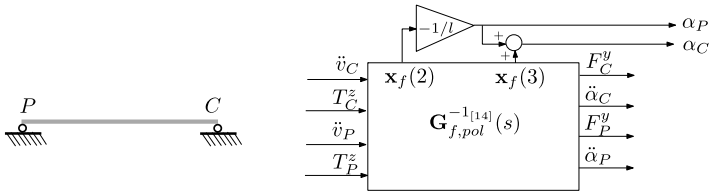


Fig. 21 The pinned–pinned beam (*left*) and its block-diagram model (*right*)

Table 7 The first two natural frequencies ω_i of the pinned–pinned beam model $\mathbf{G}_{f,\text{pol}}^{-1_{[1,4]}}(s)$ and the relative errors with the reference values $\omega_{i,\text{ref}}$

i	$\omega_{i,\text{ref}}(\sqrt{\frac{EI_z}{\rho Sl^4}})$	$\omega_i(\sqrt{\frac{EI_z}{\rho Sl^4}})$	$\Delta\omega_i$ (%)
1	9.8696	9.8725	0.03
2	39.478	39.646	0.4

Case 6: sliding–free beam (Fig. 22) The model $\mathbf{G}_{f,\text{pol}}^{-1_3}(s)$ is used to set to zero its inputs F_c^y, T_c^z, F_P^y, and $\ddot{\alpha}_P$. The augmented model with the rigid mode is depicted in Fig. 22 (right).

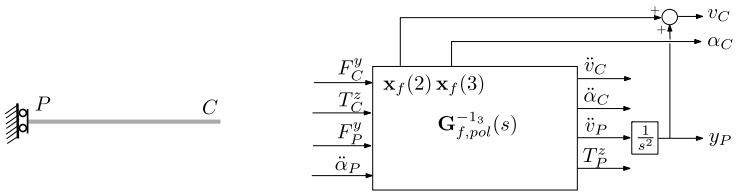


Fig. 22 The sliding–free beam (*left*) and its block-diagram model (*right*)

Table 8 The first two natural frequencies ω_i of the sliding–free beam model $\mathbf{G}_{f,\text{pol}}^{-1_3}(s)$ and the relative errors with the reference values $\omega_{i,\text{ref}}$

i	$\omega_{i,\text{ref}}(\sqrt{\frac{EI_z}{\rho Sl^4}})$	$\omega_i(\sqrt{\frac{EI_z}{\rho Sl^4}})$	$\Delta\omega_i$ (%)
1	5.5932	5.5934	0.003
2	30.226	30.734	1.7

Case 7: sliding–clamped beam (see Fig. 23) The model $\mathbf{G}_{f,\text{pol}}^{-1_{[1,2,3]}}(s)$ is used to set to zero its inputs $\ddot{v}_C$, $\ddot{\alpha}_C$, F_P^y, and $\ddot{\alpha}_P$. There are no rigid modes in this case. The internal state constraints

$$\tilde{v}'(l) = \mathbf{x}_f(3) = 0 \; \forall t \Rightarrow \dot{\mathbf{x}}_f(3) = \dot{\mathbf{x}}_f(7) = 0$$

can be used to reduce the state-space representation of $\mathbf{G}_{f,\text{pol}}^{-1_{[1,2,3]}}(s)$ to a sixth-order model.

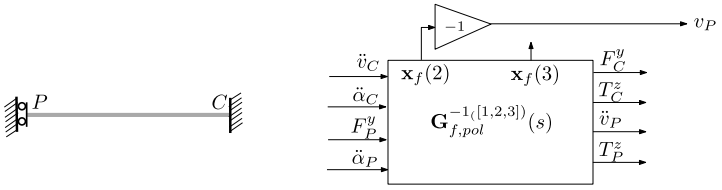


Fig. 23 The sliding–clamped beam (*right*) and its block-diagram model (*left*)

Table 9 The first two natural frequencies ω_i of the sliding–clamped beam model $\mathbf{G}_{f,\text{pol}}^{-1[1,2,3]}(s)$ and the relative errors with the reference values $\omega_{i,\text{ref}}$

i	$\omega_{i,\text{ref}}(\sqrt{\frac{EI_z}{\rho Sl^4}})$	$\omega_i(\sqrt{\frac{EI_z}{\rho Sl^4}})$	$\Delta\omega_i$ (%)
1	5.5932	5.5933	0.002
2	30.226	30.561	1.1

Case 8: sliding–pinned beam (see Fig. 24) The model $\mathbf{G}_{f,\text{pol}}^{-1[1,3]}(s)$ is used to set to zero its inputs $\ddot{v}_C$, T_C^z, F_P^y, and $\ddot{\alpha}_P$. There are no rigid modes in this case.

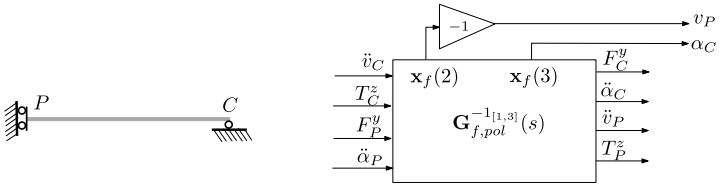


Fig. 24 The sliding–pinned beam (*right*) and its block-diagram model (*left*)

Table 10 The first two natural frequencies ω_i of the sliding–pinned beam model $\mathbf{G}_{f,\text{pol}}^{-1[1,3]}(s)$ and the relative errors with the reference values $\omega_{i,\text{ref}}$

i	$\omega_{i,\text{ref}}(\sqrt{\frac{EI_z}{\rho Sl^4}})$	$\omega_i(\sqrt{\frac{EI_z}{\rho Sl^4}})$	$\Delta\omega_i$ (%)
1	2.4674	2.4674	0.0
2	22.207	22.272	0.3

Case 9: sliding–sliding beam (Fig. 25) The model $\mathbf{G}_{f,\text{pol}}^{-1[2,3]}(s)$ is used to set to zero its inputs F_c^y, $\ddot{\alpha}_c$, F_P^y, and $\ddot{\alpha}_P$. The augmented model with the rigid mode is depicted in Fig. 25 (right).

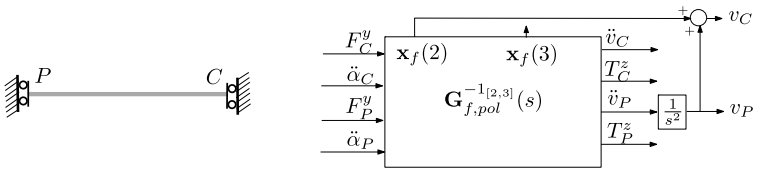


Fig. 25 The sliding–sliding beam (*left*) and its block-diagram model (*right*)

Table 11 The first two natural frequencies ω_i of the sliding–sliding beam model $\mathbf{G}_{f,\text{pol}}^{-1[2,3]}(s)$ and the relative errors with the reference values $\omega_{i,\text{ref}}$

i	$\omega_{i,\text{ref}}(\sqrt{\frac{EI_z}{\rho Sl^4}})$	$\omega_i(\sqrt{\frac{EI_z}{\rho Sl^4}})$	$\Delta\omega_i$ (%)
1	9.8696	9.8697	0.0008
2	39.478	40.988	3.8

References

1. Alazard, D., Perez, J.A., Cumer, C., Loquen, T.: Two-input two-output port model for mechanical systems. In: AIAA SciTech, American Institute of Aeronautics and Astronautics (2015). doi:10.2514/6.2015-1778
2. Bishop, R., Johnson, D.: The Mechanics of Vibration. Cambridge University Press, Cambridge (1979)

3. Craig, R.R., Chang, C.J.: Substructure coupling for dynamic analysis and testing. NASA contractor report 2781. National Aeronautics and Space Administration (1977)
4. De Luca, A., Siciliano, B.: Closed-form dynamic model of planar multilink lightweight robots. IEEE Trans. Syst. Man Cybern. **21**(4), 826–839 (1991). doi:10.1109/21.108300
5. Dokainish, M.A.: A new approach for plate vibrations: combination of transfer matrix and finite-element technique. J. Eng. Ind. **94**(2), 526–530 (1972). doi:10.1115/1.3428185
6. Euler–Bernoulli beam theory. https://en.wikipedia.org/wiki/Euler-Bernoulli_beam_theory. Accessed: 2015-09-30
7. Girard, A., Roy, N.: Dynamics of Structure in Industry. Lavoisier, Paris (2003)
8. Guy, N., Alazard, D., Cumer, C., Charbonnel, C.: Dynamic modeling and analysis of spacecraft with variable tilt of flexible appendages. Journal of Dynamic Systems Measurement and Control **136**(2) (2014). http://oatao.univ-toulouse.fr/11016/
9. Kitis, L., Lindenberg, R.: Natural frequencies and mode shapes of flexible mechanisms by a transfer matrix method. Finite Elem. Anal. Des. **6**(4), 267–285 (1990). doi:10.1016/0168-874X(90)90020-F
10. Krauss, R.W., Book, W.J.: Transfer matrix modeling of systems with noncollocated feedback. J. Dyn. Syst. Meas. Control **132**(6), 061301 (2010). doi:10.1115/1.4002476
11. Leckie, F., Pestel, E.: Transfer-matrix fundamentals. Int. J. Mech. Sci. **2**, 137–167 (1960)
12. Mohan, A., Saha, S.: A recursive, numerically stable, and efficient simulation algorithm for serial robots with flexible links. Multibody Syst. Dyn. **21**(1), 1–35 (2009). doi:10.1007/s11044-008-9122-6
13. Mucino, V.H., Pavelic, V.: An exact condensation procedure for chain-like structures using a finite element-transfer matrix approach. J. Mech. Des. **103**(2), 295–303 (1981). doi:10.1115/1.3254907
14. Murali, H., Alazard, D., Massotti, L., Ankersen, F., Toglia, C.: Mechanical-attitude controller co-design of large flexible space structures. In: Bordeneuve-Guibé, J., Drouin, A., Roos, C. (eds.) Advances in Aerospace Guidance, Navigation and Control, pp. 659–678. Springer, Berlin (2015). doi:10.1007/978-3-319-17518-8_38
15. Pascal, M.: Dynamics analysis of a system of hinge-connected flexible bodies. Celest. Mech. **41**, 253–274 (1988)
16. Perez, J.A., Alazard, D., Loquen, T., Cumer, C., Pittet, C.: Linear dynamic modeling of spacecraft with open-chain assembly of flexible bodies for ACS/structure co-design. In: Bordeneuve-Guibé, J., Drouin, A., Roos, C. (eds.) Advances in Aerospace Guidance, Navigation and Control, pp. 639–658. Springer, Berlin (2015). doi:10.1007/978-3-319-17518-8_37
17. Perez, J.A., Pittet, C., ALazard, D., Loquen, T., Cumer, C.: A flexible appendage model for use in integrated control/structure spacecraft design. IFAC-PapersOnLine **48**(9), 275–280 (2015). doi:10.1016/j.ifacol.2015.08.096
18. Perez, J.A., Alazard, D., Loquen, T., Pittet, C., Cumer, C.: Flexible multibody system linear modeling for control using component modes synthesis and double-port approach. J. Dyn. Syst. Meas. Control (2016). doi:10.1115/1.4034149
19. Rong, B., Rui, X., Wang, G.: Modified finite element transfer matrix method for eigenvalue problem of flexible structures. J. Appl. Mech. **78**(2), 021016 (2010). doi:10.1115/1.4002578
20. Rui, X., Wang, G., Lu, Y., Yun, L.: Transfer matrix method for linear multibody system. Multibody Syst. Dyn. **19**(3), 179–207 (2008). doi:10.1007/s11044-007-9092-0
21. Schiehlen, W.: Multibody system dynamics: roots and perspectives. Multibody Syst. Dyn. **1**(2), 149–188 (1997). doi:10.1023/A:1009745432698
22. Shabana, A.: Flexible multibody dynamics: review of past and recent developments. Multibody Syst. Dyn. **1**(2), 189–222 (1997). doi:10.1023/A:1009773505418
23. Shigley, J., Uicker, J.: Theory of Machines and Mechanisms. McGraw-Hill Series in Mechanical Engineering. McGraw-Hill, New York (1980). https://books.google.com.et/books?id=hkhSAAAAMAAJ
24. Simeon, B.: On Lagrange multipliers in flexible multibody dynamics. Comput. Methods Appl. Mech. Eng. **195**(50–51), 6993–7005 (2006). Multibody Dynamics Analysis. doi:10.1016/j.cma.2005.04.015
25. Sitti, M.: Piezoelectrically actuated four-bar mechanism with two flexible links for micromechanical flying insect thorax. IEEE/ASME Trans. Mechatron. **8**(1), 26–36 (2003). doi:10.1109/TMECH.2003.809126
26. Sylla, M., Asseke, B.: Dynamics of a rotating flexible and symmetric spacecraft using impedance matrix in terms of the flexible appendages cantilever modes. Multibody Syst. Dyn. **19**, 345–364 (2008). doi:10.1007/s11044-007-9102-2
27. Tan, T., Yousuff, A., Bahar, L., Konstantinidis, M.: A modified finite element-transfer matrix for control design of space structures. Comput. Struct. **36**(1), 47–55 (1990). doi:10.1016/0045-7949(90)90173-Y
28. Theodore, R.J., Ghosal, A.: Comparison of the assumed modes and finite element models for flexible multilink manipulators. Int. J. Robot. Res. **14**(2), 91–111 (1995). http://dblp.uni-trier.de/db/journals/ijrr/ijrr14.html#TheodoreG95
29. Turcic, D.A., Midha, A.: Dynamic analysis of elastic mechanism systems. Part I: applications. J. Dyn. Syst. Meas. Control **106**(4), 249–254 (1984). doi:10.1115/1.3140681